BJ www.biochemj.org

Biochem. J. (2012) **441**, 1017–1026 (Printed in Great Britain) doi:10.1042/BJ20111659

online data

Crystallographic and X-ray absorption spectroscopic characterization of *Helicobacter pylori* UreE bound to Ni^{2+} and Zn^{2+} reveals a role for the disordered C-terminal arm in metal trafficking

Katarzyna BANASZAK*[1], Vlad MARTIN-DIACONESCU†[1], Matteo BELLUCCI‡, Barbara ZAMBELLI‡, Wojciech RYPNIEWSKI*, Michael J. MARONEY† and Stefano CIURLI‡§[2]

*Institute of Bioorganic Chemistry, Polish Academy of Sciences, Noskowskiego 12/14, 61-704 Poznan, Poland, †Department of Chemistry, University of Massachusetts, Amherst, MA 01003, U.S.A., ‡Laboratory of Bioinorganic Chemistry, Department of Agro-Environmental Science and Technology, University of Bologna, Viale G. Fanin 40, 40127 Bologna, Italy, and §Center for Magnetic Resonance (CERM), University of Florence, Via Luigi Sacconi 6, I-50019 Sesto Fiorentino, Italy

The survival and growth of the pathogen *Helicobacter pylori* in the gastric acidic environment is ensured by the activity of urease, an enzyme containing two essential Ni^{2+} ions in the active site. The metallo-chaperone UreE facilitates *in vivo* Ni^{2+} insertion into the apoenzyme. Crystals of apo-*Hp*UreE (*H. pylori* UreE) and its Ni^{2+}- and Zn^{2+}-bound forms were obtained from protein solutions in the absence and presence of the metal ions. The crystal structures of the homodimeric protein, determined at 2.00 Å (apo), 1.59 Å (Ni^{2+}) and 2.52 Å (Zn^{2+}) resolution, show the conserved proximal and solvent-exposed His^{102} residues from two adjacent monomers invariably involved in metal binding. The C-terminal regions of the apoprotein are disordered in the crystal, but acquire significant ordering in the presence of the metal ions due to the binding of His^{152}. The analysis of X-ray absorption spectral data obtained using solutions of Ni^{2+}- and Zn^{2+}-bound *Hp*UreE provided accurate information of the metal-ion environment in the absence of solid-state effects. These results reveal the role of the histidine residues at the protein C-terminus in metal-ion binding, and the mutual influence of protein framework and metal-ion stereo-electronic properties in establishing co-ordination number and geometry leading to metal selectivity.

Key words: metal-ion selectivity, metallo-chaperone, metal trafficking, protein crystallography, urease assembly, X-ray absorption spectroscopy.

INTRODUCTION

Urease [1,2] is a Ni^{2+}-dependent enzyme that plays a crucial role in the nitrogen cycle by catalysing the hydrolysis of urea to ammonia and carbamate with a 3×10^{15}-fold rate enhancement with respect to the uncatalysed reaction [3] (Scheme 1).

The active site contains two Ni^{2+} ions that are bridged by a post-translationally carbamylated lysine residue and a hydroxide ion, and are bound to the protein framework by four histidine imidazole nitrogen atoms and one aspartate residue carboxylate oxygen atom [4–7]. The co-ordination geometry of the Ni^{2+} ions is completed by labile water molecules, yielding one penta-co-ordinated Ni^{2+} ion with a distorted square-pyramidal geometry, and one hexa-co-ordinated Ni^{2+} ion with a distorted octahedral geometry (Scheme 2).

Urease is initially produced in the apo form, devoid of Ni^{2+} ions and enzymatic activity. The apo-enzyme is modified in several successive steps that require a dedicated set of accessory proteins, usually comprising UreD, UreF, UreG and UreE. [8] This process leads to carbamylation of the active-site lysine and incorporation of the binuclear metallic active site, with consequent enzyme activation (Scheme 2). The activity of urease is strictly required for the survival and growth of bacterial pathogens that colonize human and animal gastric mucosa as well as intestinal and urinary tracts, and therefore both the enzyme and the accessory proteins represent targets for drug development [9,10]

The urease activation process entails the formation of a multimeric complex between the apoenzyme and UreD, UreF and UreG, with the latter protein probably responsible for lysine carbamylation following GTP hydrolysis. UreE appears to act as a metallo-chaperone by delivering Ni^{2+} to the UreDFG complex [11–13]. This role for UreE is supported by the evidence that the concentration of Ni^{2+} required for proper assembly of the urease active site is considerably reduced, and a larger amount of enzyme is activated, in the presence of UreE [14]. Another crucial role for UreE is the enhancement of the GTPase activity of UreG [13], which relies on the direct UreE–UreG interaction shown to occur *in vivo* and *in vitro* [15,16].

Recombinant UreE proteins from different sources, including *Ka*UreE (*Klebsiella aerogenes* UreE) [17], *Bp*UreE (*Bacillus pasteurii* UreE) [18] and *Hp*UreE (*Helicobacter pylori* UreE) [19], have been structurally characterized. These orthologues consistently exhibit a homodimeric architecture composed of an N-terminal domain and a C-terminal domain, the latter mediating head-to-head dimerization. A conserved metal-binding site involves a pair of closely spaced histidine residues, one per monomer, located on the protein surface at the homodimer interface (His^{96} in *Ka*UreE, His^{100} in *Bp*UreE and His^{102} in *Hp*UreE).

Despite sharing common structural features, UreE proteins have different metal-binding capabilities. In particular, they exhibit a variable stoichiometry for Ni^{2+}-binding that ranges from one

Abbreviations used: *Bp*UreE, *Bacillus pasteurii* UreE; EXAFS, extended X-ray absorption fine structure; *Hp*UreE, *Helicobacter pylori* UreE; ITC, isothermal titration calorimetry; *Ka*UreE, *Klebsiella aerogenes* UreE; MAD, multiwavelength anomalous dispersion; rmsd, root mean square deviation; XANES: X-ray absorption near-edge spectroscopy.

[1] These authors contributed equally to this work.

[2] To whom correspondence should be addressed (email stefano.ciurli@unibo.it).

The structural co-ordinates reported will appear in the PDB under accession codes 3TJA, 3TJB and 3TJ9.

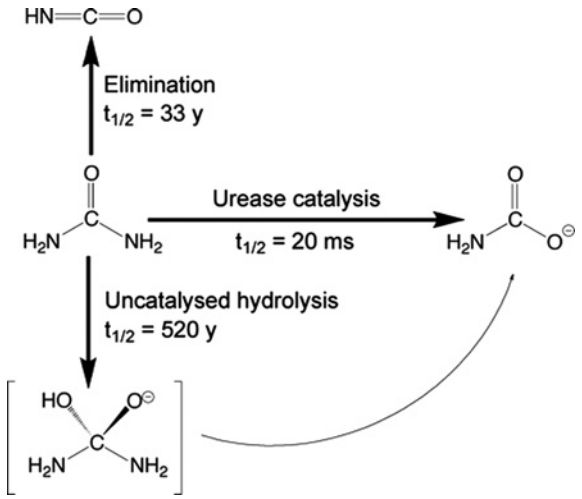

Scheme 1 Mechanisms of urea decomposition in water

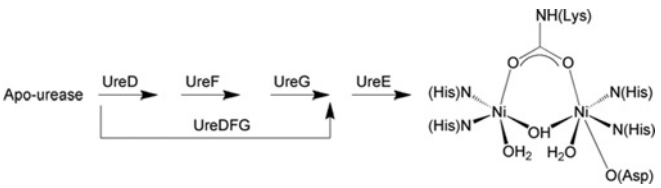

Scheme 2 Activation of urease and building of the nickel-containing active site

metal ion bound per dimer for *Hp*UreE [15,20] to six ions for *Ka*UreE [21], with two Ni^{2+} ions bound in the case of *Bp*UreE [22]. Interestingly, this peculiarity is reflected by the nature of their C-terminal regions. *Ka*UreE, possessing the highest Ni^{2+}-sequestering activity, features a histidine-rich tail containing ten histidine residues among the last fifteen amino acids. *Bp*UreE displays two C-terminal histidine residues at the end of its sequence, in the context of a His-Gln-His motif, whereas in this region *Hp*UreE contains a single histidine residue (His^{152}) [23].

All UreE proteins contain at least one histidine residue in the C-terminal portion, an observation that suggested a role for the C-terminus in modulating the metal-trafficking activity of UreE proteins, in terms of both selectivity and stoichiometry of metal binding [15,22,23]. However, the structural and functional details of these regions are not well established. The crystal structure of *Ka*UreE (PDB codes 1GMW, 1GMU and 1GMV) was determined on a truncated form of this protein (H144**Ka*UreE) that lacks the last 15 residues [17], whereas the crystal structure of *Bp*UreE (PDB codes 1EAR and 1EBO) showed a solid-state disorder that prevented the observation of the Gly-His-Gln-His motif at the C-terminus [18]. The recently described structures of *Hp*UreE (PDB codes 3L9Z, 3NXZ, 3NYO and 3LA0) in the apo form or bound to Cu^{2+}, Ni^{2+} or an unidentified metal ion cover only residues 1/2–148/149 and therefore do not include His^{152} [19]. The only exception is the tetrameric (dimer of dimers) form of Ni-*Hp*UreE, which features a square pyramidal Ni^{2+} site composed of four His^{102} residues (one from each protomer) in the basal plane and a single His^{152} in the axial position [19]. However, this type of tetrameric arrangement, even though observed commonly in the solid state probably because of the elevated concentrations utilized for protein crystallization, does not correspond to the simple dimeric form of the protein present in solution, as established using static and dynamic light scattering [15,22].

The present study describes the crystal structures of recombinant *Hp*UreE in the apo, Ni^{2+}-bound and Zn^{2+}-bound forms. These structures reveal the architecture of the C-terminal arm and the metal-binding mode of the His^{152} residue located in this region. The structures, determined in the solid state, were corroborated by X-ray absorption spectroscopy in frozen solutions of the wild-type and the H152A *Hp*UreE mutant proteins in the presence of bound Ni^{2+} and Zn^{2+}, providing accurate metric parameters in the vicinity of the metal ions. The results of the present study clarify the role of the protein framework for Ni^{2+} and Zn^{2+} trafficking effected by UreE within the urease activation process.

EXPERIMENTAL

Protein crystallization

Recombinant apo-*Hp*UreE was purified as described previously [15]. Crystallization trials were carried out using the hanging-drop vapour-diffusion method. Crystals of the apoprotein were obtained by mixing 2 μl of an 8 mg/ml protein solution in Tris/HCl buffer, pH 7, with a reservoir solution containing 0.1 M sodium citrate, pH 5.6, 0.5 M ammonium sulfate and 1.0 M lithium sulfate. Cuboidal crystals appeared within 2 weeks. Crystals of Zn-*Hp*UreE were obtained by mixing 2 μl of an 8 mg/ml protein solution in Tris/HCl buffer, pH 7, containing an equimolar amount of Zn^{2+} ($ZnSO_4$), with 2 μl of a reservoir solution made of 4.0 M sodium formate and 0.1 M sodium cacodylate, pH 6.5. Crystals with a hexagonal cross-section formed within 2 weeks. Crystals of Ni-*Hp*UreE were obtained by mixing 2 μl of an 8 mg/ml protein solution in Tris/HCl buffer, pH 7, containing an equimolar amount of Ni^{2+} ($NiSO_4$), with 2 μl of a reservoir solution made of 4.0 M sodium formate and 0.1 M sodium acetate, pH 5.5. One block-shaped crystal appeared after approximately 30 days.

X-ray diffraction data collection, structure determination and refinement

X-ray diffraction data were recorded on the BL14.1 and BL14.2 beam lines at BESSY (Berlin Electron Storage Ring Company for Synchrotron Radiation) (Berlin, Germany) at 100 K in the presence of 20 % (v/v) glycerol or 4.0 M sodium formate as a cryo-protectant. Data collection and refinement statistics are summarized in Table 1.

Three datasets for the Zn-*Hp*UreE crystal were collected in a MAD (multiwavelength anomalous dispersion) experiment in the 2.52–2.77 Å resolution range (1 Å = 0.1 nm). The images were processed with the HKL package [24] using an 'anomalous' option during scaling. The Zn-*Hp*UreE structure was solved with a three-wavelength MAD protocol in Auto-Rickshaw [25]. Heavy-atom searching was performed with SHELXD [26], and the resulting positions were refined with phase calculation using SHARP [27]. The density modification and phase extension were performed using DM [28] and RESOLVE [29]. An initial model was built using ARP/wARP [30,31]. Heavy-atom analysis based on the initial model, together with phasing and building cycles, were performed using PHASER [32], MLPHARE [33], SHELXE [34], RESOLVE [29] and BUCCANEER [33]. Three heavy-atom sites were detected, which included two Zn^{2+} ions and the sulfur atom of Cys^{95}. Initially, 598 residues from the four protomers in the asymmetric unit were found by automatic modelling, followed by manual model building and refinement using REFMAC [35].

One dataset at 1.59 Å resolution was recorded for the Ni-*Hp*UreE crystal. The data were processed with the HKL package [24]. The structure was solved by molecular replacement using

Table 1 X-ray diffraction data collection and refinement statistics

Values in parentheses are for the highest-resolution shell.

	Zn-*Hp*UreE			Ni-*Hp*UreE	Apo-*Hp*UreE
Data collection					
Beamline	BESSY BL14.2			BESSY BL14.2	BESSY BL14.1
Temperature (K)	100			100	100
	Peak	Inflection	Remote		
Wavelength (Å)	1.28183	1.28316	1.27655	0.91885	0.91841
Space group	$P6_522$			$C222_1$	$P2_12_12_1$
Cell constants (Å)					
a	109.34			67.55	69.00
b	109.34			117.14	70.47
c	280.34			98.66	123.34
Resolution (Å)	50.00–2.52 (2.56–2.52)	50.00–2.59 (2.63–2.59)	50.00–2.77 (2.82–2.77)	50.00–1.59 (1.62–1.59)	20.00–2.00 (2.03–2.00)
R_{sym}	0.092 (0.434)	0.095 (0.586)	0.100 (0.558)	0.049 (0.448)	0.060 (0.593)
$I / \sigma(I)$	22.4 (3.4)	21.5 (2.3)	20.8 (2.3)	24.9 (2.6)	21.6 (2.0)
Completeness (%)	99.9 (98.2)	99.7 (95.9)	99.5 (92.9)	97.9 (87.7)	99.7 (96.6)
Redundancy	9.4 (6.9)	9.1 (5.2)	9.0 (4.9)	8.4 (3.2)	5.5 (4.9)
Refinement					
Resolution (Å)	2.52			1.59	2.00
No. of reflections	33219			48955	38745
R_{work}/R_{free}	0.203/0.245			0.185/0.210	0.208 / 0.267
Number of protein atoms	4697			2402	4734
Number of metal atoms	2			1	0
Number of water molecules	186			154	100
Average B-factor for protein atoms (Å^2)	43.815			33.694	44.327
Average B-factor for metal atoms (Å^2)	37.275			28.650	–
Rmsd of bond lengths (Å)	0.021			0.031	0.022
Rmsd of bond angles (°)	1.909			2.578	1.947
PDB code	3TJ9			3TJ8	3TJA

Table 2 Final sample concentrations used for EXAFS analysis of *Hp*UreE wild-type and H152A mutant

Sample	Protein (mM)	Ni^{2+} (mM)	Zn^{2+} (mM)
Ni-*Hp*UreE	0.53	0.48	
Zn-*Hp*UreE	0.53		0.48
H152A Ni-*Hp*UreE	0.77	0.69	
H152A Zn-*Hp*UreE	0.22		0.19

PHASER [32] with one chain of Zn-*Hp*UreE as the search model. Solutions were found that corresponded to two *Hp*UreE protomers in the asymmetric unit. The atomic model was refined using REFMAC [35].

One dataset at 2.00 Å resolution was recorded for the apo-*Hp*UreE crystal. The data were processed with the HKL package [24]. The structure was solved by molecular replacement using PHASER [32], with one chain of Ni-*Hp*UreE as the search model. Four apo-*Hp*UreE protomers were found in the asymmetric unit. The atomic model was refined using REFMAC [35].

X-ray absorption spectroscopy sample preparation

Metal ions (0.9 equivalents) as sulfate salts were added to stock solutions of wild-type *Hp*UreE dimer (0.60 mM) and H152A-*Hp*UreE dimer (0.25 mM for Zn^{2+} and 0.87 mM for Ni^{2+}) to prepare Zn^{2+}- and Ni^{2+}-bound protein samples. Final sample concentrations are listed in Table 2. Samples were prepared in 20 mM Tris/HBr buffer at pH 7, containing 150 mM NaBr. The protein samples were incubated for 5 min upon metal addition, loaded into sample cells consisting of a polycarbonate sample holder with a kapton window, and frozen in liquid N_2. The samples were stored at $-80\,^{\circ}C$ and transported in liquid N_2 before being used at the synchrotron beam line. On the basis of established K_d values and protein concentrations [15], less than 2 % of the Ni^{2+} and Zn^{2+} added should be dissociated under these conditions.

X-ray absorption spectroscopy data collection and analysis

Datasets were collected at SSRL (Stanford Synchrotron Radiation Lightsource; 3 GeV ring) beam line 9-3 equipped with a 100-element Ge X-ray fluorescence detector array (Canberra). The only exception is the H152A *Hp*UreE Ni^{2+} sample, which was run at beam line 7-3 using a 30-element Ge detector. Both stations consisted of a Si(220) $\varphi = 0\,^{\circ}$ double-crystal monochromator, and a liquid helium cryostat for the sample chamber. Söller slits were used to reduce scattering and 3 μm Z-1 element filters were placed between the sample and the detector. Internal energy calibration was performed by collecting spectra simultaneously in transition mode on the relevant metal foil (Zn or Ni).

Data averaging and energy calibration was performed using SixPack [36]. The first inflection points from the XANES (X-ray absorption near-edge spectroscopy) spectral regions were set to 9660.7 eV for Zn foil (Zn samples) and to 8331.6 eV for Ni foil (Ni samples). The AUTOBK algorithm available in the Athena software package was employed for data reduction and normalization [37]. A linear pre-edge function followed by a quadratic polynomial for the post-edge was used for background subtraction followed by normalization of the edge-jump.

Data limits were chosen to maximize resolution and signal-to-noise ratio. The Zn-*Hp*UreE EXAFS (extended X-ray absorption fine structure) data were extracted using an R_{bkg} of 0.9 and a spline with a range for k of 2–13.5 Å^{-1}, with a rigid spline clamp at higher k. The k^3-weighted data were fitted in r-space over the k range 2–13.5 Å^{-1} using an E_0 of 9670 eV. The Ni-*Hp*UreE EXAFS data were extracted using an R_{bkg} of 1, and a

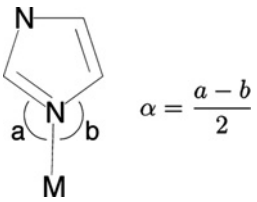

Figure 1 Definition of the α angle involving histidine imidazole and bound metal ion M

spline from $k = 2$ Å^{-1} to $k = 13.5$ Å^{-1} with a strong clamp at high k values for wild-type *Hp*UreE, and a spline from $k = 2$ Å^{-1} to $k = 12.5$ Å^{-1} with a rigid clamp at higher k values for H152A *Hp*UreE. The k^3-weighted data were fitted in r-space over the $k = 2$–13.5 Å^{-1} region for wild-type *Hp*UreE and $k = 2$–12.5 Å^{-1} for the mutant, with E_0 for Ni^{2+} set to 8340 eV in both cases. All datasets were processed using a Kaiser–Bessel window with a dk of 2 (window sill).

Artemis software employing the FEFF6 and IFEFFIT algorithms was used to generate and fit scattering paths to the data [37–39]. Single-scattering and multiple-scattering fits were performed as described in subsequent sections. Single-scattering fits were generally carried out over an r-space of 1–2.0 (and up to 2.5) Å, whereas multiple-scattering fits were generated over the 1–4.0 (and up to 4.2) Å range of r-space, as specified in Supplementary Tables S1–S8 at http://www.BiochemJ.org/bj/441/bj4411017add.htm. Average values and bond lengths obtained from crystallographic data were used to construct rigid imidazole rings to fit histidine residues [40]. The position of the imidazole ring with respect to the metal centre was fitted in terms of the metal–ligand bond distance (R_{eff}) and the rotation angle α (Figure 1) [41,42].

To assess the goodness-of-fit from different fitting models, the *R*-factor, χ^2 and reduced χ^2 (χ_ν^2) were minimized. Increasing the number of adjustable parameters is generally expected to improve the *R*-factor; however, χ_ν^2 may go through a minimum and then increase, indicating that the model is over-fitting the data. These parameters are defined as follows:

$$\chi^2 = \frac{N_{idp}}{N_{pts}\varepsilon^2}\sum_{i=1}^{N}(\{\mathrm{Re}[\chi_{data}(R_i) - \chi_{theory}(R_i)]\}^2 + \{\mathrm{Im}[\chi_{data}(R_i) - \chi_{theory}(R_i)]\}^2)$$

and:

$$\chi_\nu^2 = \frac{\chi^2}{(N_{idp} - N_{var})}$$

where N_{idp} is the number of independent data points defined as:

$$N_{idp} = \frac{2\Delta r \Delta k}{\pi}$$

where Δr is the fitting range in *r*-space, Δk is the fitting range in *k*-space, N_{pts} is the number of points in the fitting range, N_{var} is the number of variables floating during the fit, ε is the measurement uncertainty, Re() is the real part of the EXAFS Fourier-transformed data and theory functions, Im() is the imaginary part of the EXAFS Fourier-transformed data and theory functions, $\chi(R_i)$ is the Fourier-transformed data or theory function and:

$$R = \frac{\sum_{i=1}^{N}(\{\mathrm{Re}[\chi_{data}(R_i) - \chi_{theory}(R_i)]\}^2 + \{\mathrm{Im}[\chi_{data}(R_i) - \chi_{theory}(R_i)]\}^2)}{\sum_{i=1}^{N}(\{\mathrm{Re}[\chi_{data}(R_i)]\}^2 + \{\mathrm{Im}[\chi_{data}(R_i)]\}^2)}$$

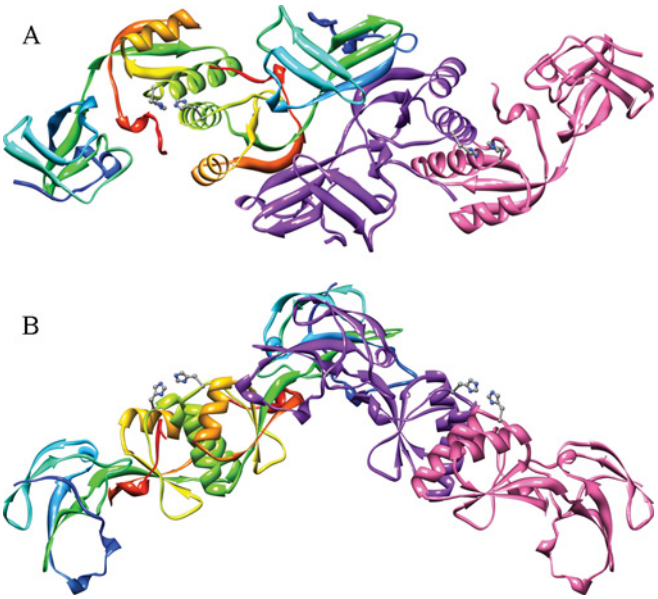

Figure 2 Crystal structure of apo-*Hp*UreE

Ribbon schemes of the crystallographic structural model of the apo-*Hp*UreE dimer of dimers in the asymmetric unit. (**B**) Representation of the same structure in (**A**) rotated by 90° about the horizontal axis. Each of the protomers forming the dimer on the left is coloured from blue in the proximity of the N-terminus to red at the C-terminus in order to highlight the secondary structure elements along the protein sequence. The dimer on the right shows the two protomers in different colours (purple and pink). The side chains of the conserved His^{102} are represented as ball-and-stick models coloured according to the CPK (Corey–Panling–Koltun) colour code.

RESULTS

X-ray crystallography on *Hp*UreE in the apo and holo forms bound to Ni^{2+} and Zn^{2+}

Three crystal structures have been analysed: *Hp*UreE in the apo form at 2.00 Å resolution (apo-*Hp*UreE), the protein co-crystallized with Ni^{2+} at 1.59 Å resolution (Ni-*Hp*UreE), and the protein co-crystallized with Zn^{2+}, solved at 2.52 Å resolution (Zn-*Hp*UreE). Each structure is in a different crystal form.

The crystals of the apoprotein are orthorhombic, $P2_12_12_1$, with four polypeptide chains assembled into two dimers in the asymmetric unit (Figure 2). Each chain was modelled starting from the N-terminal methionine residue, but at the C-termini the last 20–22 residues are disordered and therefore invisible. Unambiguous electron density extends to Ser^{149} in chain A, to Met^{150} in chains B and D, and to Val^{148} in chain C.

The Ni-*Hp*UreE crystals are orthorhombic, $C222_1$, with one protein dimer and one Ni^{2+} ion in the asymmetric unit (Figure 3). Amino acid residues were modelled from Met^1 to His^{149} for chain A and from Met^1 to His^{152} for chain B.

The Zn-*Hp*UreE crystals are hexagonal, $P6_522$, and contain two protein dimers and two Zn^{2+} ions in the asymmetric unit (Figure 4). The polypeptide chains were modelled from the N-terminal Met^1. Chains B and C could be traced to residue Ser^{153} and Glu^{154} respectively. Chains A and D were modelled to Ser^{149}, whereas the electron density from residues 150 to154 is unclear and has been interpreted as statically disordered residues (see below). In addition, the electron density in chain D is disordered from Leu^{13} to Ser^{19} and from Lys^{65} to Ile^{71}.

The polypeptide fold is similar to the previously reported crystal structures of *Ka*UreE [17] (PDB codes 1GMW, 1GMU and 1GMV), *Bp*UreE [18] (PDB codes 1EAR and 1EB0) and *Hp*UreE

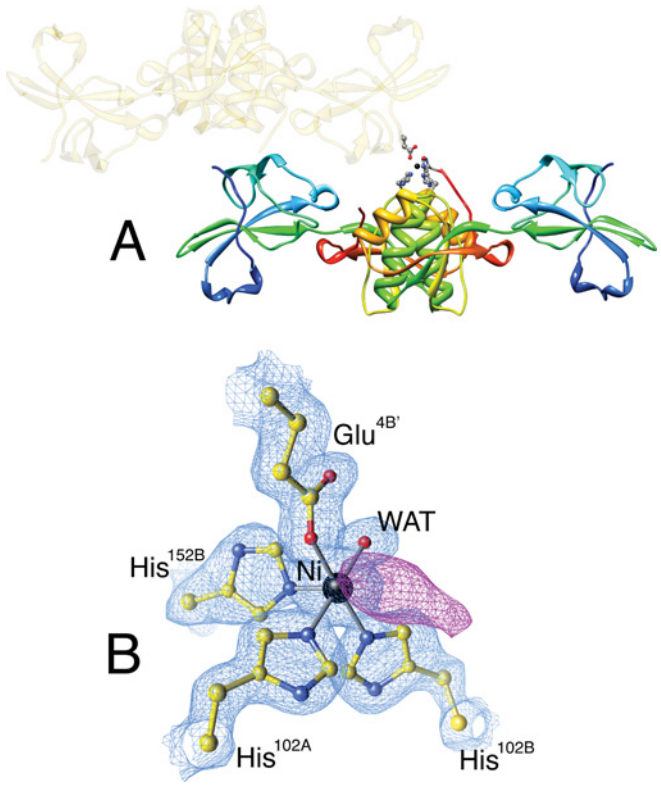

Figure 3 Crystal structure of Ni-*Hp*UreE

(**A**) Ribbon scheme of the crystallographic structural model of the Ni-*Hp*UreE dimer in the asymmetric unit, with each protomer coloured from blue in the proximity of the N-terminus to red at the C-terminus in order to highlight the secondary structure elements along the protein sequence. The symmetry-related dimer that carries the $Glu^{4B'}$ residue bound to Ni^{2+} (represented as a black sphere) is shown as transparent gold ribbon. The side chains of the Ni-bound ligands His^{102A}, His^{102B}, His^{152B} and $Glu^{4B'}$, as well as the solvent molecule, are represented as ball-and-stick models coloured according to the CPK (Corey–Pauling–Koltun) colour code. (**B**) Close-up view of the co-ordination environment of the Ni^{2+} ion together with the $2F_o–F_c$ electron density map contoured at 1.5 σ (light blue) and the $F_o–F_c$ electron density map contoured at 3.0 σ (magenta).

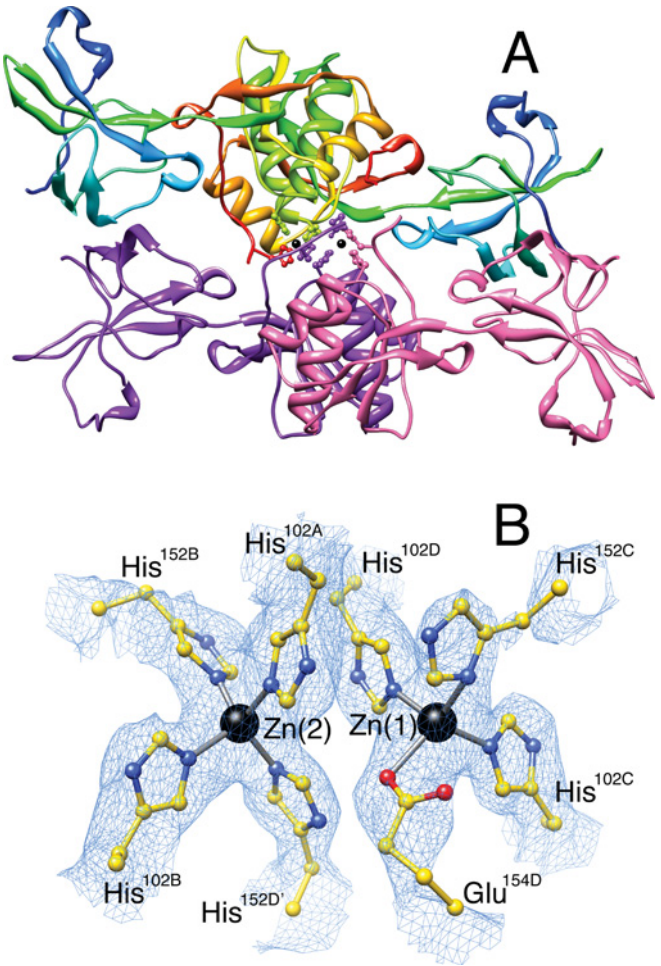

Figure 4 Crystal structure of Zn-*Hp*UreE

Ribbon scheme of the crystallographic structural model of the Zn-*Hp*UreE dimer of dimers in the asymmetric unit. Each protomer of the dimer on the top is coloured from blue in the proximity of the N-terminus to red at the C-terminus in order to highlight the secondary structure elements along the protein sequence. The dimer on the bottom shows the two protomers in different colours (purples and pink). The side chains of the histidine residues binding the Zn^{2+} ions (shown as black spheres) are represented as ball-and-stick models coloured according to their position in the sequence and in the protomer. (**B**) Close-up view of the co-ordination environment of the Zn^{2+} ions together with the $2F_o–F_c$ electron density map contoured at 1.0 σ (light blue).

[19] (PDB codes 3L9Z, 3NXZ, 3NY0 and 3LA0). Each protein subunit contains two domains (Figures 2–4). The N-terminal domain includes residues from Met^1 to Asp^{77} and consists of two three-stranded mixed β-sheets with two extended loops connecting strands 1 and 2, and strand 2 with strand 3. Each of the two loops contains a β-turn. The C-terminal domain includes residues from Ser^{78} and has a ferredoxin-like $\beta\alpha\beta\beta\alpha\beta$ fold. Residues Glu^{144}–Leu^{146} form a short fifth β-strand and the last ordered residues stretch along the two α-helices of the other subunit of the dimer. The segment from Ser^{149} to Glu^{154} is poorly ordered but interpretable in Zn-*Hp*UreE, whereas the remaining residues, up to the C-terminal Lys^{170}, are not visible in the electron density.

The proteins in the three crystal structures form dimers. The core of their interface is formed by two α-helices (residues 88–102) running in parallel. Each helix is braced on the other side by a segment of residues 146–150 from the other subunit. Both hydrophobic and hydrogen-bonded interactions occur between the two helices, and between the helices and neighbouring residues and the poorly ordered C-terminal stretch, with a notable hydrophobic cluster formed by pairs of Val^{88} and Val^{91} from the two subunits. Symmetric inter-subunit hydrogen bonds are found between Tyr^{96} and Ala^{103}, Asn^{100} and His^{102}, Ala^{89} and Gln^{111}, and Glu^{97} and Ser^{149}.

The Ni^{2+} ion in Ni-*Hp*UreE co-ordinates six ligands arranged in a pseudo-octahedral co-ordination geometry (Figure 3). It interacts with His^{102A}, His^{102B}, His^{152B}, $Glu^{4B'}$ (a residue located on chain B of a symmetry-related molecule), one water molecule and another unidentified ligand (Figure 5A). The electron density of this moiety is elongated, and therefore it is unlikely to be a water molecule (Figure 3B). It could be His^{152A}, but there is no continuity in the electron density between this ligand density and the nearby Ser^{149A}, which is the last visible residue of chain A. This implies a disordered chain comprising residues 150 and 151. The role of $Glu^{4B'}$ in forming a dimer of dimers is probably a solid-state effect since only dimers (not tetramers) are observed in solution using multi-angle scattering [15,22], and this dangling Ni^{2+} ligand could easily be replaced by a water molecule in solution.

In Zn-*Hp*UreE, each of the two Zn^{2+} ions have four ligands arranged in a pseudo-tetrahedral co-ordination geometry (Figure 4B). Zn(1) interacts with His^{102C}, His^{102D}, His^{152C} and

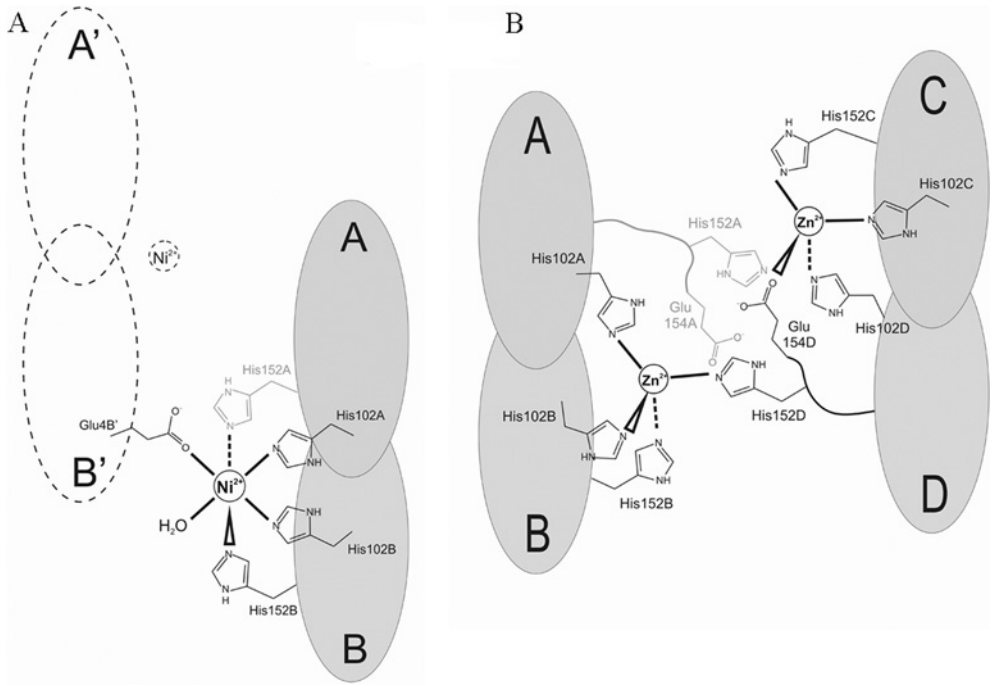

Figure 5 Schematic depiction of the ligand environments around the metal ions in Ni-*Hp*UreE and Zn-*Hp*UreE

(**A**) Interaction of the Ni^{2+} with six ligands in the Ni-*Hp*UreE structure. The A/B dimer is shown in grey, and the symmetry-related dimer A'/B' is shown by broken lines. The ambiguous interaction with His^{152A} is indicated with a grey line. (**B**) Interactions of the two Zn^{2+} ions with four ligands each in the Zn-*Hp*UreE structure. Dimers A/B and C/D are shown in grey. The alternative interactions with His^{152A} and Glu^{154A} are shown using a grey line.

a partially disordered Glu^{154D}, whereas Zn(2) is bound by His^{102A}, His^{102B}, His^{152B} and the partially disordered His^{152D} from the neighbouring C/D dimer (Figure 5B). The electron density corresponding to the segment His^{152D}–Glu^{154D} suggests an alternative interpretation, with the side chain of His^{152A} taking the place of Glu^{154D}, and Glu^{154A} replacing His^{152D}. The first alternative seems to have a higher occupancy factor, but some residual density indicates that the second alternative also occurs in the crystal.

All of the subunits of the apo and metal-bound *Hp*UreE models were superposed using the Cα atoms. The rmsd (root-mean-square deviation) values ranged from 0.6 to 1.1 Å. The number of outliers, pairs of atoms deviating more than 3 rmsd, ranged from zero to nine. A comparison with the previously determined structures of UreE from *H. pylori* (PDB codes 3MY0 and 3L9Z) gave similar statistics. Comparing the two apo-*Hp*UreE dimers or the two Zn^{2+} dimers present in the asymmetric unit gave a similarly good fit (0.8–0.9 Å, with zero and three outliers respectively). Significantly larger differences were observed only when apo-*Hp*UreE dimers were compared with metal-loaded dimers (rmsd 1.3–1.4 Å with 30–66 outliers) and when Zn^{2+}-bound dimers were compared with Ni^{2+}-bound dimers (rmsd 0.9 Å with 48 outliers), with the largest differences observed in the outer (C-terminal) domains of the dimer.

X-ray absorption spectroscopy on the Ni^{2+}-binding site in wild-type and H152A *Hp*UreE

The Ni *K*-edge XANES spectra of both the wild-type and H152A mutant Ni-*Hp*UreE samples exhibit a single intense white line at ~8347 eV, and a small pre-edge peak that is associated with a 1s→3d transition at 8331.6 eV, consistent with a six-co-ordinate Ni^{2+}-binding site and octahedral geometry (Figure 6A) [43]. The difference between the spectra obtained for wild-type and the mutant *Hp*UreE samples arises from the nature of the ligands involved, as revealed by the analysis of the EXAFS spectra (see Supplementary Tables S1–S4 at http://www.BiochemJ.org/bj/441/bj4411017add.htm).

The best multiple-scattering fits of the wild-type Ni-*Hp*UreE (Supplementary Tables S1 and S2) are consistent with the presence of four histidine residues around the Ni^{2+} centre, spread over two shells of N/O-donor ligands (Figure 6B). The features between 2 and 4 Å are best described using a combination of histidine ligands with an angle α of 5° and 10°, separated in two scattering shells. At 2.06(2) Å, a shell is formed by a pair of histidine residues with an angle α of 10° and two N/O ligands. The second shell consists of an additional two histidine residues ($\alpha = 5°$) at 2.15(1) Å (Table 3, Figure 6B and Supplementary Table S2). The separation between the two shells of ~0.09(3) Å is at the limit of the resolution (~0.1 Å) for the dataset. Splitting the histidine residues into two shells significantly improves the goodness-of-fit, although the reduced χ^2 only drops by a factor of 1.3 (compared with an optimal factor of 1.7). Such a two-shell model is consistent with the wild-type *Hp*UreE Ni^{2+}-binding site described by the crystallographic data in the present study, as well as theoretical models [15]. Both studies show the presence of two distinct sets of histidine residues at the Ni^{2+} site in the wild-type *Hp*UreE dimer, the His^{102} pair and the His^{152} pair, where the His^{102} pair is essential for metal binding.

A weakening of the Ni^{2+} complex formation was observed upon mutagenesis of His^{152}, with the dissociation constant increasing from 0.15 μM in the wild-type protein to 0.89 μM in the H152A mutant [15]. EXAFS analysis of the H152A Ni^{2+} site indeed reveals a significant change in the co-ordination environment, which could explain the change in the binding constants. The best fit of the EXAFS spectra for the H152A *Hp*UreE mutant suggests the presence of only two co-ordinating histidine residues around

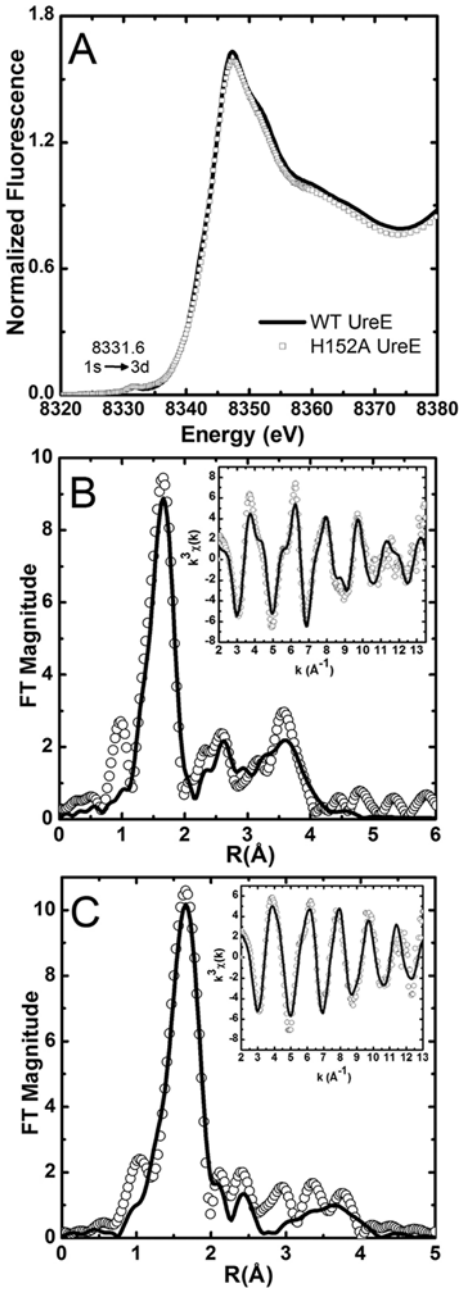

Figure 6 X-ray absorption spectroscopic analysis of *Hp*UreE at the Ni *K*-edge

(**A**) Ni *K*-edge XANES spectra of wild-type (WT) and H152A Ni-*Hp*UreE. (**B**) Fourier-transformed Ni *K*-edge EXAFS spectra of wild-type Ni-*Hp*UreE [no phase correction, Fourier transform (FT) window = 2–13.5 Å^{-1}]. The inset shows the k^3-weighted unfiltered EXAFS spectra: data (black line), best fit (white circles). (**C**) Fourier-transformed Ni *K*-edge EXAFS spectra of H152A Ni-*Hp*UreE (no phase correction, FT window = 2–12.5 Å^{-1}). The inset shows the k^3-weighted unfiltered EXAFS spectra: data (black line), best fit (white circles).

Ni^{2+}, together with four other N/O-donor ligands (Figure 6C and Table 3). Although still six-co-ordinate, the H152A *Hp*UreE Ni^{2+}-binding site is best fitted using a single shell of ligands, as evident from single-scattering fits (Supplementary Table S3). The multiple-scattering analysis (Supplementary Table S4) shows that this shell contains only two histidine residues, presumably His^{102}, with an angle α of 10°. This shell is complemented by four additional N/O-donor ligands at 2.09(1) Å. Therefore it is

Table 3 Best fit EXAFS models

WT, wild-type.

Sample	Ligand*	*r* (Å)	σ^2 ($\times 10^3$ Å^2)	%*R*	χ_ν^2
WT Ni-*Hp*UreE	2 N_{His}^{10}	2.15(2)	3(1)	3.8	36.6
	2 N_{His}^{5}	2.06(1)	2.5(7)		
	2 N/O	2.06(1)	2.5(7)		
H152A Ni-*Hp*UreE	2 N_{His}^{10}	2.09(1)	3.7(5)	5.2	32.4
	4 N/O	2.09(1)	3.7(5)		
WT Zn-*Hp*UreE	2 N_{His}^{5}	1.99(2)	5(1)	3.78	17.3
	2 N/O	2.07(3)	12(5)		
	1 Br	2.38(1)	4.3(4)		
	2 N_{His}^{5}	2.00(1)	4(1)	2.61	12.8
	1 N_{His}^{5}	2.16(1)	1(1)		
	1 N/O	2.00(1)	3(2)		
	1 Br	2.39(1)	4.8(5)		
H152A Zn-*Hp*UreE	2 N_{His}^{5}	2.01(1)	6.7(5)	1.85	3.96
	2 N/O	2.01(1)	6.7(5)		
	1 Br	2.39(1)	3.4(2)		

*The superscripted number is the angle α for the histidine ligands.

plausible that upon mutating the more weakly bound histidine residues [His^{152} most probably occurring at 2.15(1) Å in the wild-type *Hp*UreE] there is a rearrangement in the Ni^{2+}-binding site of *Hp*UreE resulting in changes in the orientation of His^{102} to facilitate Ni^{2+} co-ordination by an additional pair of N/O-donor ligands that compensate for the removal of His^{152}.

X-ray absorption spectroscopy on the Zn^{2+}-binding site in wild-type and H152A mutant *Hp*UreE

The differences in the Zn *K*-edge XANES spectra of wild-type and H152A Zn-*Hp*UreE (Figure 7A) bound to one Zn^{2+} equivalent are not significant and are consistent with a four- or five-co-ordinate Zn^{2+} site. The normalized fluorescence intensity approaches 1.5 at its maximum, which favours a five-co-ordinate over a four-co-ordinate binding site [44]. Furthermore, the lack of resolution among the post-edge XANES features suggests that Zn^{2+} co-ordination is dominated by N/O donors [44].

The EXAFS spectrum of wild-type Zn-*Hp*UreE is distinct from the Ni^{2+} complex and shows two features in the Fourier-transformed spectrum that indicate the presence of two scattering shells. For biological samples, this is consistent with a shell of N/O-donor ligands at 1.5 Å (in r-space, uncorrected for phase shifts), and a second shell of sulfur/halogens ligands at 2.0 Å [45]. Single-scattering fits suggest the presence of a bromide ligand in addition to five N/O donors (see Supplementary Table S5 at http://www.BiochemJ.org/bj/441/bj4411017add.htm). Features between 2.5 and 4 Å in r-space are generally attributed to histidine residues. Two models for wild-type Zn-*Hp*UreE emerge from the multiple-scattering analysis. The best-fit model consists of three histidine residues arranged in two shells (Figure 7B). The first shell at 2.00(1) Å consists of an N/O-donor ligand in addition to two histidine ligands with $\alpha = 5°$. The second shell at 2.16(1) Å consists of a single histidine residue and an N/O-donor ligand, whereas a third shell contains a bromide ion at 2.39(1) Å. This model is in agreement with the crystallographically determined dimer-of-dimer wild-type Zn-*Hp*UreE crystal structure, which indicates that at least three histidine residues play a role in Zn^{2+} co-ordination. Modelling the EXAFS with four histidine ligands did not improve the fit (see Supplementary Table S6 at http://www.BiochemJ.org/bj/441/bj4411017add.htm). Although the model with three histidine ligands described above gives the best fit in terms of both goodness-of-fit (*R*-factor) and reduced χ^2,

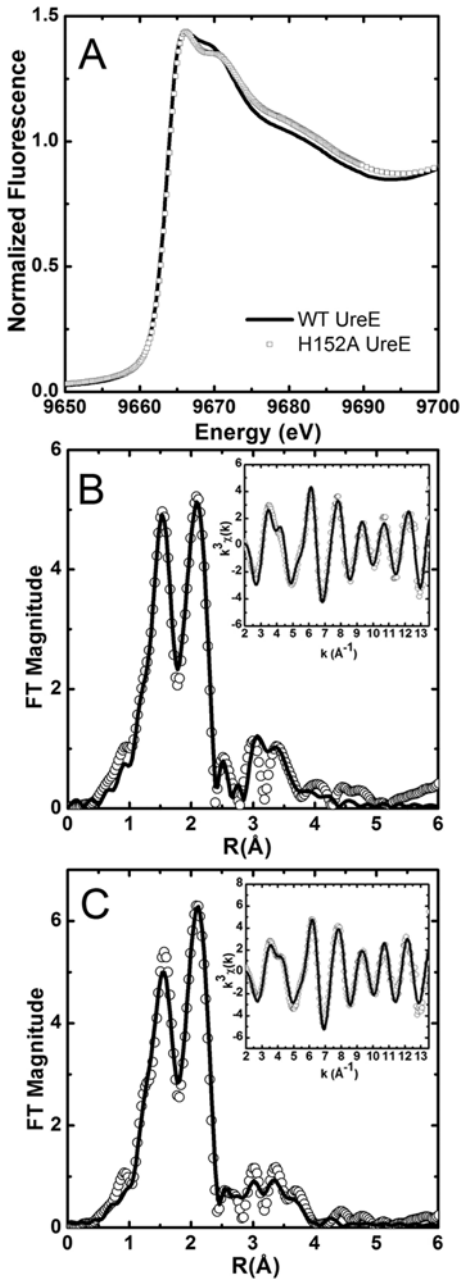

Figure 7 X-ray absorption spectroscopic analysis at *Hp*UreE at the Zn *K*-edge

(**A**) Zn *K*-edge XANES spectra of wild-type (WT) and H152A Zn-*Hp*UreE. (**B**) Fourier-transformed EXAFS spectra of wild-type Zn-*Hp*UreE [no phase correction, Fourier transform (FT) window = 2–13.5 Å^{-1}]. The inset shows the k^3-weighted unfiltered EXAFS spectra: data (black line), best fit (white circles). (**C**) Fourier-transformed Zn *K*-edge EXAFS spectra of H152A Zn-*Hp*UreE (no phase correction, FT window = 2–13.5 Å^{-1}). The inset shows the k^3-weighted unfiltered EXAFS spectra: data (black line), best fit (white circles).

it is not statistically distinct from a second model with only two histidine ligands (Table 3). The difference in reduced χ^2 for the two models differ by only a factor of 1.4, and not the optimal 1.8 that would allow the two-histidine model to be ruled out.

Removal of the His^{152} pair in the H152A mutant *Hp*UreE results in a Zn^{2+}-binding site that is also five-co-ordinate and has a bound bromide at 2.39(1) Å. However, only two histidine residues are readily simulated in the EXAFS analysis, which together with two other N/O-donor ligands, form a scattering shell at 2.01(1) Å (Table 3, Figure 7C and Supplementary Tables S7 and S8 at http://www.BiochemJ.org/bj/441/bj4411017add.htm).

In summary, the best descriptions of the metal-binding sites from XAS analysis indicate that in wild-type *Hp*UreE the Ni^{2+} site is six-co-ordinate with six N/O-donors, of which four are histidine ligands, and the Zn^{2+} site is five-co-ordinate with two or three histidine ligands and a bromide ion. In H152A *Hp*UreE, a six-co-ordinate $(N/O)_6Ni$ site is retained, but includes only two HisN-donor ligands. Similarly, the corresponding Zn^{2+} site in H152A *Hp*UreE retains a five-co-ordinate $(N/O)_4Br$ site that is similar to the wild-type Zn^{2+} site, but contains only two HisN-donor ligands.

DISCUSSION

The present study represents an attempt to clarify the role of the disordered C-terminal portions of the two protomers in homodimeric UreE proteins in the metal binding and release steps that occur when UreE acts as a metallo-chaperone in the process of Ni^{2+} insertion in the urease active site. A role for the C-terminal protein region was initially suggested in the case of *Bp*UreE by metal-binding experiments coupled with X-ray absorption spectroscopy, which indicated the presence of a binuclear Ni^{2+}-binding site involving the fully conserved His^{100} as well as the C-terminal histidine residues [22]. Subsequently, ITC (isothermal titration calorimetry) coupled with site-directed mutagenesis indicated that binding of a single Zn^{2+} or Ni^{2+} ion to the homodimeric *Hp*UreE involves His^{102} on the protein surface, and that mutation of His^{152} on the disordered C-terminal arm alters the metal-binding properties of the protein [15]. Although Ni^{2+} is essential for enzymatic activity, being present in the active site of the functional urease enzyme, Zn^{2+} has been found to mediate and stabilize the interaction between *H. pylori* UreE and UreG *in vitro* [15]. UreG is another accessory protein with a GTPase role in the metallocentre assembly, suggesting a possible functional role for Zn^{2+}, in addition to Ni^{2+}, in this process [15]. So far, structural information on the Ni^{2+} and Zn^{2+} metal-binding environment of the homodimeric functional form of UreE has been hindered by protein oligomerization, occurring in the solid state, coupled with the molecular disorder of the *Hp*UreE C-terminal region, which is known to be involved in metal binding on the basis of solution studies. In particular, although the crystal structure of apo-UreE from *H. pylori* was determined to be a dimer, the metal-bound form was described as a tetramer, or a dimer of dimers, with one metal ion bound between the four protein subunits [19]. A similar tetrameric arrangement was observed around a single Zn^{2+} ion in a structural study of *Bp*UreE [18]. These observations prompted us to investigate further the Ni^{2+}- and Zn^{2+}-binding properties of *Hp*UreE both in the solid state, using X-ray crystallography, and in solution, using X-ray absorption spectroscopy. This multifaceted approach yields consistent results that are in agreement with previous calorimetric studies, and reveals the structural details of the co-ordination environment of a single Ni^{2+} or Zn^{2+} ion bound to a single protein homodimer. The key role played by the conserved histidine ligands in the C-terminal arm of each protomer is thus demonstrated, and the protein motif is observed to gain significant structural ordering upon metal binding.

A comparison of all the *Hp*UreE models (two apo dimers, two Zn^{2+}-bound dimers and one Ni^{2+}-bound dimer from the present study, as well as the previously reported apo and Ni^{2+}-bound structures) indicates some flexibility of the protein through the linker chain connecting the central domain. The central domain consists of two C-terminal halves of the protein, dimerizing head-to-head, and two peripheral N-terminal domains. On the basis of

temperature factors and rmsd values, the most mobile parts of the models are the loops between strands 1 and 2 and between strands 5 and 6 on the surface of the N-terminal domain. The most disordered region is found towards the end of the C-terminal region, which, in the best case, becomes untraceable in electron density maps after residue Gly^{154}.

In the crystal structures presented herein, a single metal ion (Ni^{2+} or Zn^{2+}) is found per protein dimer, in agreement with the stoichiometry previously obtained using ITC [15]. This metal ion is co-ordinated by two His^{102} residues, one from each UreE monomer subunit. This arrangement, suggestive of a pair of tweezers, holds the metal cation on the surface of the protein dimer. The rest of the co-ordination environment involves the C-terminal segment, which is in contact with the metal ions through His^{152}. This protein region is not visible in the apo-protein, but becomes significantly more ordered upon metal binding. Nevertheless, some disorder in the electron density was still observed. The data suggest that the *Hp*UreE binding arrangement, stable on one side and transient on the other, can be easily disengaged, and thus represents a fine balance between binding the metal ion and releasing it to its partners, a balance that is necessary for the chaperone function of UreE in Ni^{2+} trafficking.

In the crystal structure, the co-ordination of the Zn^{2+} site is tetrahedral, whereas the Ni^{2+} ion adopts an axially elongated distorted octahedral site that is approximately square bipyramidal. This reflects the intrinsic co-ordination preferences of the two metal ions, with Zn^{2+} being d^{10} and closed-shell, having no stereo-electronic preferences and leading to a co-ordination number and geometry imposed only by steric constraints, whereas Ni^{2+}, being d^8 and open-shell, has stereo-electronic preferences towards a tetragonal 4+2 co-ordination geometry due to the ligand field stabilization energy. The ability of the different cations to achieve their preferred co-ordination number in the complex with UreE indicates a significant flexibility of the protein. Indeed, the angle His^{102} Nε2–Ni^{2+}–His^{102} Nε2 is close to 90° and it becomes 106–109° with Zn^{2+}. The other ligands also appear in appropriate positions and numbers. The arrangement of the protein around the Ni^{2+} ion is more open. In addition to the pair of His^{102} residues and a pair of His^{152}, the Ni^{2+} ion takes two additional ligands (a water molecule and Glu$^{4'}$ from a neighbouring protein molecule in the crystal lattice). The Zn^{2+} is surrounded by the two pairs of histidine residues, His^{102} and His^{152} (with one of the latter histidine ligands possibly displaced by Glu^{154D}).

Conclusions

The structural features of *Hp*UreE established in the present study allow us to propose a role for the C-terminal portions of the UreE dimer in molecular recognition and metal-ion delivery. In particular, the observations strongly support the idea that UreE could exist in two different conformations. In a 'closed' state, the delivered metal ion would be bound to the protein through the two conserved His^{102} residues (*H. pylori* numbering) and to histidine residues invariably found in the C-terminal region of this class of proteins (His^{152} in the case of *Hp*UreE). The C-terminal region, disordered in the absence of the metal, but gaining order upon metal binding, would change into an 'open' state when protein–protein interactions between UreE and a partner protein, or protein complex, prone to receive the metal ion are present. In this form, His^{152} and analogous residues would be replaced with amino acid residues located on the surface of the protein partner receiving the metal ion from UreE.

Different roles of *Hp*UreE bound to Ni^{2+} and Zn^{2+} are suggested by the observation that Zn^{2+}, but not Ni^{2+}, stabilizes the interaction between *Hp*UreE and its cognate GTPase *Hp*UreG [15]. The cross-talk between UreE, Ni^{2+} and Zn^{2+} suggests a specific functional role for different metal complexes of this urease accessory protein in regulating the formation of protein–protein complexes involved in enzyme maturation. The present study has shown that the metal-ion selectivity of UreE is based on the different metal-ion co-ordination environments that are dictated by the electronic properties of the metal ion in a mechanism that is facilitated by the flexibility of the C-terminal protein region.

AUTHOR CONTRIBUTION

Matteo Bellucci and Barbara Zambelli expressed and purified HpUreE and its mutants. Katarzyna Banaszak carried out protein crystallization, X-ray diffraction data collection and processing, protein structure solution, refinement and analysis. Vlad Martin-Diaconescu carried out X-ray absorption data collection and analysis. Wojciech Rypniewski, Michael Maroney and Stefano Ciurli designed the study and interpreted the data. All authors contributed to writing and editing the paper, and approved the final version of the paper.

ACKNOWLEDGEMENTS

We acknowledge the Helmholtz-Zentrum Berlin – Electron storage ring BESSY II for provision of synchrotron radiation at beamlines 14.1 and 14.2. Portions of this research were carried out at the Stanford Synchrotron Radiation Lightsource (SSRL), a national user facility operated by Stanford University on behalf of the U.S. Department of Energy, Office of Basic Energy Sciences.

FUNDING

This work was supported by the European Community's Seventh Framework Programme (FP7/2007-2013) [grant number 226716 (to W.R.)]; the National Institutes of Health [grant number R01-GM-69696 (to M.M.)]; and the Italian Ministero dell'Istruzione, dell'Università e della Ricerca PRIN2007 (to S.C.). The SSRL Structural Molecular Biology Program is supported by the Department of Energy, Office of Biological and Environmental Research, and by the National Institutes of Health National Center for Research Resources Biomedical Technology Program.

REFERENCES

1 Carter, E. L., Flugga, N., Boer, J. L., Mulrooney, S. B. and Hausinger, R. P. (2009) Interplay of metal ions and urease. Metallomics **1**, 207–221
2 Zambelli, B., Musiani, F., Benini, S. and Ciurli, S. (2011) Chemistry of Ni^{2+} in urease: sensing, trafficking, and catalysis. Acc. Chem. Res. **44**, 520–530
3 Callahan, B. P., Yuan, Y. and Wolfenden, R. (2005) The burden borne by urease. J. Am. Chem. Soc. **127**, 10828–10829
4 Jabri, E., Carr, M. B., Hausinger, R. P. and Karplus, P. A. (1995) The crystal structure of urease from *Klebsiella aerogenes*. Science **268**, 998–1004
5 Benini, S., Rypniewski, W. R., Wilson, K. S., Miletti, S., Ciurli, S. and Mangani, S. (1999) A new proposal for urease mechanism based on the crystal structures of the native and inhibited enzyme from *Bacillus pasteurii*: why urea hydrolysis costs two nickels. Structure **7**, 205–216
6 Ha, N.-C., Oh, S.-T., Sung, J. Y., Cha, K. A., Lee, M. H. and Oh, B.-H. (2001) Supramolecular assembly and acid resistance of *Helicobacter pylori* urease. Nat. Struct. Biol. **8**, 505–509
7 Balasubramanian, A. and Ponnuraj, K. (2010) Crystal structure of the first plant urease from jack bean: 83 years of journey from its first crystal to molecular structure. J. Mol. Biol. **400**, 274–283
8 Quiroz, S., Kim, J. K., Mulrooney, S. B. and Hausinger, R. P. (2007) Chaperones of nickel metabolism. In Nickel and its Surprising Impact in Nature (Sigel, A., Sigel, H. and Sigel, R. K.O., eds), pp. 519–544, John Wiley & Sons, Chichester
9 Mobley, H. L. T. and Hausinger, R. P. (1989) Microbial urease: significance, regulation and molecular characterization. Microbiol. Rev. **53**, 85–108
10 Mobley, H. L. T., Island, M. D. and Hausinger, R. P. (1995) Molecular biology of microbial ureases. Microbiol. Rev. **59**, 451–480
11 Park, I.-S. and Hausinger, R. P. (1996) Metal ion interactions with urease and UreD–urease apoproteins. Biochemistry **35**, 5345–5352
12 Park, I. S. and Hausinger, R. P. (1995) Requirement of carbon dioxide for *in vitro* assembly of the urease nickel metallocenter. Science **267**, 1156–1158

13 Soriano, A., Colpas, G. J. and Hausinger, R. P. (2000) UreE stimulation of GTP-dependent urease activation in the UreD–UreF–UreG–urease apoprotein complex. Biochemistry **39**, 12435–12440
14 Lee, M. H., Mulrooney, S. B., Renner, M. J., Markowicz, Y. and Hausinger, R. P. (1992) *Klebsiella aerogenes* urease gene cluster: sequence of ureD and demonstration that four accessory genes (ureD, ureE, ureF, ureG) are involved in nickel metallocenter biosynthesis. J. Bacteriol. **174**, 4324–4330
15 Bellucci, M., Zambelli, B., Musiani, F., Turano, P. and Ciurli, S. (2009) *Helicobacter pylori* UreE, a urease accessory protein: specific Ni^{2+} and Zn^{2+} binding properties and interaction with its cognate UreG. Biochem. J. **422**, 91–100
16 Boer, J. L., Quiroz-Valenzuela, S., Anderson, K. L. and Hausinger, R. P. (2010) Mutagenesis of *Klebsiella aerogenes* UreG to probe nickel binding and interactions with other urease-related proteins. Biochemistry **49**, 5859–5869
17 Song, H.-K., Mulrooney, S. B., Huber, R. and Hausinger, R. P. (2001) Crystal structure of *Klebsiella aerogenes* UreE, a nickel-binding metallochaperone for urease activation. J. Biol. Chem. **276**, 49359–49364
18 Remaut, H., Safarov, N., Ciurli, S. and Van Beeumen, J. (2001) Structural basis for Ni^{2+} transport and assembly of the urease active site by the metallochaperone UreE from *Bacillus pasteurii*. J. Biol. Chem. **276**, 49365–49370
19 Shi, R., Munger, C., Asinas, A., Benoit, S. L., Miller, E., Matte, A., Maier, R. J. and Cygler, M. (2010) Crystal structures of apo and metal-bound forms of the UreE protein from *Helicobacter pylori*: role of multiple metal binding sites. Biochemistry **49**, 7080–7088
20 Benoit, S. and Maier, R. J. (2003) Dependence of *Helicobacter pylori* urease activity on the nickel-sequestering ability of the UreE accessory protein. J. Bacteriol. **185**, 4787–4795
21 Lee, M. Y., Pankratz, H. S., Wang, S., Scott, R. A., Finnegan, M. G., Johnson, M. K., Ippolito, J. A., Christianson, D. W. and Hausinger, R. P. (1993) Purification and characterization of *Klebsiella aerogenes* UreE protein: a nickel binding protein that functions in urease metallocenter assembly. Protein Sci. **2**, 1042–1052
22 Stola, M., Musiani, F., Mangani, S., Turano, P., Safarov, N., Zambelli, B. and Ciurli, S. (2006) The nickel site of *Bacillus pasteurii* UreE, a urease metallo-chaperone, as revealed by metal-binding studies and X-ray absorption spectroscopy. Biochemistry **45**, 6495–6509
23 Musiani, F., Zambelli, B., Stola, M. and Ciurli, S. (2004) Nickel trafficking: insights into the fold and function of UreE, a urease metallochaperone. J. Inorg. Biochem. **98**, 803–813
24 Otwinowski, Z. and Minor, W. (1997) Processing of X-ray diffraction data collected in oscillation mode. Methods Enzymol. **276**, 307–325
25 Panjikar, S., Parthasarathy, V., Lamzin, V. S., Weiss, M. S. and Tucker, P. A. (2005) Auto-Rickshaw: an automated crystal structure determination platform as an efficient tool for the validation of an X-ray diffraction experiment. Acta Crystallogr. Sect. D Biol. Crystallogr. **61**, 449–457
26 Schneider, T. R. and Sheldrick, G. M. (2002) Substructure solution with SHELXD. Acta Crystallogr. Sect. D Biol. Crystallogr. **58**, 1772–1779
27 de la Fortelle, E. and Bricogne, G. (1997) Maximum-likelihood heavy-atom parameter refinement for the MIR and MAD methods. Methods Enzymol. **276**, 472–494
28 Cowtan, K. (1994) An automated procedure for phase improvement by density modification. Joint CCP4 ESF-EACBM Newsl. Protein Crystallogr. **31**, 34–38
29 Terwilliger, T. C. (2000) Maximum-likelihood density modification. Acta Crystallogr. Sect. D Biol. Crystallogr. **56**, 965–972
30 Perrakis, A., Morris, R. and Lamzin, V. S. (1999) Automated protein model building combined with iterative structure refinement. Nat. Struct. Biol. **6**, 458–463
31 Morris, R. J., Zwart, P. H., Cohen, S., Fernandez, F. J., Kakaris, M., Kirillova, O., Vonrhein, C., Perrakis, A. and Lamzin, V. S. (2004) Breaking good resolutions with ARP/wARP. J. Synchrotron Radiat. **11**, 56–59
32 McCoy, A. J., Grosse-Kunstleve, R. W., Adams, P. D., Winn, M. D., Storoni, L. C. and Read, R. J. (2007) Phaser crystallographic software. J. Appl. Crystallogr. **40**, 658–674
33 Collaborative Computational Project, Number 4 (1994) The CCP4 suite: programs for protein crystallography Acta Crystallogr. Sect. D Biol. Crystallogr. **50**, 760–763
34 Sheldrick, G. M. (2002) Macromolecular phasing with SHELXE. Z. Kristallogr. **217**, 644–650
35 Murshudov, G. N., Vagin, A. A. and Dodson, E. J. (1997) Refinement of macromolecular structures by the maximum-likelihood method. Acta Crystallogr. Sect. D Biol. Crystallogr. **53**, 240–255
36 Webb, S. M. (2005) Sixpack: a graphical user interface for XAS analysis using IFEFFIT. Physica Scripta **T115**, 1011–1014
37 Ravel, B. and Newville, M. (2005) ATHENA, ARTEMIS, HEPHAESTUS: data analysis for X-ray absorption spectroscopy using IFEFFIT. J. Synchrotron Radiat. **12**, 537–541
38 Zabinsky, S. I., Rehr, J. J., Ankudinov, A., Albers, R. C. and Eller, M. J. (1995) Multiple scattering calculations of x-ray absorption spectra. Phys. Rev. B **52**, 2995–3009
39 Newville, M. (2001) EXAFS analysis using FEFF and FEFFIT. J. Synchrotron Radiat. **8**, 96–100
40 Engh, R. A. and Huber, R. (1991) Accurate bond and angle parameters for X-ray protein structure refinement. Acta Crystallogr. Sect. A Found. Crystallogr. **47**, 392–400
41 Blackburn, N. J., Hasnain, S. S., Pettingill, T. M. and Strange, R. W. (1991) Copper K-extended X-ray absorption fine structure studies of oxidized and reduced dopamine β-hydroxylase. Confirmation of a sulfur ligand to copper(I) in the reduced enzyme. J. Biol. Chem. **266**, 23120–23127
42 Ferreira, G. C., Franco, R., Mangravita, A. and George, G. N. (2002) Unraveling the substrate–metal binding site of ferrochelatase: an X-ray absorption spectroscopic study. Biochemistry **41**, 4809–4818
43 Colpas, G. J., Maroney, M. J., Bagyinka, C., Kumar, M., Willis, W. S., Suib, S. L., Baidya, N. and Mascharak, P. K. (1991) X-ray spectroscopic studies of nickel complexes, with application to the structure of nickel sites in hydrogenases. Inorg. Chem. **30**, 920–928
44 Jacquamet, L., Aberdam, D., Adrait, A., Hazemann, J. L., Latour, J. M. and Michaud-Soret, I. (1998) X-ray absorption spectroscopy of a new zinc site in the Fur protein from *Escherichia coli*. Biochemistry **37**, 2564–2571
45 Strange, R. W., Blackburn, N. J., Knowles, P. F. and Hasnain, S. S. (1987) X-ray absorption spectroscopy of metal–histidine coordination in metalloproteins. Exact simulation of the EXAFS of tetrakis(imidazole)copper(II) nitrate and other copper–imidazole complexes by the use of a multiple-scattering treatment. J. Am. Chem. Soc. **109**, 7157–7162

Received 13 September 2011/20 October 2011; accepted 20 October 2011
Published as BJ Immediate Publication 20 October 2011, doi:10.1042/BJ20111659

Biochem. J. (2012) **441**, 1017–1026 (Printed in Great Britain) doi:10.1042/BJ20111659

online data

SUPPLEMENTARY ONLINE DATA

Crystallographic and X-ray absorption spectroscopic characterization of *Helicobacter pylori* UreE bound to Ni^{2+} and Zn^{2+} reveals a role for the disordered C-terminal arm in metal trafficking

Katarzyna BANASZAK*[1], Vlad MARTIN-DIACONESCU†[1], Matteo BELLUCCI‡, Barbara ZAMBELLI‡, Wojciech RYPNIEWSKI*, Michael J. MARONEY† and Stefano CIURLI‡§[2]

*Institute of Bioorganic Chemistry, Polish Academy of Sciences, Noskowskiego 12/14, 61-704 Poznan, Poland, †Department of Chemistry, University of Massachusetts, Amherst, MA 01003, U.S.A., ‡Laboratory of Bioinorganic Chemistry, Department of Agro-Environmental Science and Technology, University of Bologna, Viale G. Fanin 40, 40127 Bologna, Italy, and §Center for Magnetic Resonance (CERM), University of Florence, Via Luigi Sacconi 6, I-50019 Sesto Fiorentino, Italy

Table S1 Ni-*Hp*UreE wild-type single-scattering EXAFS fits

Fits were carried out in r-space ($\Delta k = 2$–13.5 $Å^{-1}$; $\Delta r = 1$–2.1 Å) with a Kaiser–Bessel window (d$k = 2$), k-weight = 3 and $S_0 = 0.9$. Separate sets of Δr_{eff} and σ^2 for the sulfur atoms and nitrogen atoms were used with initial values of 0.0 Å and 0.003 $Å^2$ respectively. A universal E_0 was initially set to 8340.0 eV and $\Delta E_0 = 0$ eV. Initial input metal–ligand distances were 2.0 Å for Ni–N and 2.3 Å for Ni–S. (where $\nu = N_{idp} - N_{var}$; N_{idp} = number of independent points, and N_{var} = number of variables).

Description	Fit no.	R_{factor}	${\chi^2}_\nu$	χ^2	N_{var}	N_{idp}	ν	$1+2\sqrt{2/\nu}$
N_5	1	0.0275	81.2	391.966	3	7	4	2.4
N_6	2	0.0214	63.314	305.624	3	7	4	2.4
N_7	3	0.0317	93.746	452.528	3	7	4	2.4
N_4N_1	4	0.0215	108.461	306.636	5	7	2	3.0
N_3N_2	5	0.021	105.875	299.323	5	7	2	3.0
N_5N_1	6	0.0193	97.578	275.868	5	7	2	3.0
N_4N_2	7	0.0192	96.674	273.311	5	7	2	3.0
N_3N_3	8	0.0192	96.732	273.475	5	7	2	3.0
N_6N_1	9	0.0197	99.512	281.335	5	7	2	3.0
N_5N_2	10	0.0265	133.397	377.133	5	7	2	3.0
N_4N_3	11	0.0257	129.686	366.641	5	7	2	3.0
N_3S_1	12	0.0499	251.561	711.199	5	7	2	3.0
N_1S_3	13	0.0565	284.732	804.981	5	7	2	3.0
N_2S_2	14	0.0526	265.323	750.108	5	7	2	3.0
N_4S_1	15	0.0242	121.872	344.551	5	7	2	3.0
N_3S_2	16	0.0266	133.928	378.633	5	7	2	3.0
N_2S_3	17	0.0278	140.307	396.67	5	7	2	3.0
N_5S_1	18	0.0176	88.599	250.483	5	7	2	3.0
N_1S_5	19	0.0176	88.538	250.309	5	7	2	3.0
N_2S_4	20	0.0179	90.363	255.468	5	7	2	3.0
N_4S_2	21	0.0152	76.494	216.26	5	7	2	3.0
N_3S_3	22	0.014	70.481	199.261	5	7	2	3.0

[1] These authors contributed equally to this work.
[2] To whom correspondence should be addressed (email stefano.ciurli@unibo.it).
The structural co-ordinates reported will appear in the PDB under accession codes 3TJA, 3TJB and 3TJ9.

Table S2 Ni-*Hp*UreE EXAFS fits using multiple-scattering imidazoles

Fits were carried out in r-space ($\Delta k = 2$–13.5 Å^{-1}; $\Delta r = 1$–4.2 Å) with a Kaiser–Bessel window (d$k = 2$), k-weight = 3 and $S_0 = 0.9$. All paths with an amplitude of 14% or higher and a r_{eff} value within the fitting range were included for the imidazoles. Separate sets of Δr_{eff} and σ^2 for the histidine ligands (modelled as imidazoles 'H$^{\alpha}$' where α is the angle of rotation) and nitrogen atoms were used with initial values of 0.0 Å and 0.003 Å^2 respectively; with a universal E_0 value initially set to 8340.0 eV and $\Delta E_0 = 0$ eV. Initial input metal–ligand distances were 2.0 Å for Ni–imidazole and 2.0 Å for Ni–N (where $\nu = N_{idp} - N_{var}$; N_{idp} = number of independent points, and N_{var} = number of variables).

Description	Fit no.	R_{factor}	$\chi^2{}_\nu$	χ^2	ΔE	N_{var}	N_{idp}	ν	$1+2\sqrt{2/\nu}$
$N_5H_1{}^5$	23	0.1202	104.422	2092.002		3	23	20	1.6
$N_4H_2{}^5$	24	0.0816	70.877	1419.97		3	23	20	1.6
$N_3H_3{}^5$	25	0.06	52.157	1044.923		3	23	20	1.6
$N_2H_4{}^5$	26	0.0549	47.736	956.349		3	23	20	1.6
$N_2H_4{}^5$	27	0.0529	51.058	920.785		5	23	18	1.7
$N_2H_2{}^5H_2{}^5$	28	0.0423	45.917	736.249		7	23	16	1.7
$N_2H_2{}^5H_2{}^{10}$	29	0.0357	38.708	620.648		7	23	16	1.7
$N_2H_2{}^5H_2{}^{10}$	30	0.0379	36.559	659.311		5	23	18	1.7
$N_2H_4{}^5$	26	0.0549	47.736	956.349	1.7	3	23	20	*1.6*
N	2 N/O	4 N_{His}							
r (Å)	2.08(1)	2.08(1)							
σ^2 ($\times 10^3$)	4.5(5)	4.5(5)							
$N_2H_4{}^5$	27	0.0529	51.058	920.785	1.01	5	23	18	1.7
N	2 N/O	4 N_{His}							
r (Å)	2.11(2)	2.07(1)							
σ^2 ($\times 10^3$)	4(3)	5(1)							
$N_2H_2{}^5H_2{}^5$	28	0.0423	45.917	736.249	1.81	7	23	16	1.7
N	2 N/O	2 N_{His}	2 N_{His}						
r (Å)	2.10(2)	2.15(2)	2.03(1)						
σ^2 ($\times 10^3$)	3(2)	1(2)	0(1)						
$N_2H_2{}^5H_2{}^{10}$	29	0.0357	38.708	620.648	1.17	7	23	16	1.7
N	2 N/O	2 N_{His}	2 N_{His}						
r (Å)	2.06(2)	2.06(2)	2.14(2)						
σ^2 ($\times 10^3$)	3(2)	3(2)	3(2)						
$N_2H_2{}^5H_2{}^{10}$	30	0.0379	36.559	659.311	1.67	5	23	18	1.7
N	2 N/O	2 N_{His}	2 N_{His}						
r (Å)	2.06(1)	2.06(1)	2.15(2)						
σ^2 ($\times 10^3$)	2.5(7)	2.5(7)	3(1)						

Table S3 Ni-*Hp*UreE H152A single-scattering EXAFS fits

Fits were carried out in r-space ($\Delta k = 2$–12.5 Å^{-1}; $\Delta r = 1$–2.0 Å) with a Kaiser–Bessel window (d$k = 2$), k-weight = 3 and $S_0 = 0.9$. Separate sets of Δr_{eff} and σ^2 for the sulfur atoms and nitrogen atoms were used with initial values of 0.0 Å and 0.003 Å^2 respectively. A universal E_0 was initially set to 8340.0 eV and $\Delta E_0 = 0$ eV. Initial input metal–ligand distances were 2.0 Å for Ni–N and 2.3 Å for Ni–S. (where $\nu = N_{idp} - N_{var}$ and N_{idp} = number of independent points; N_{var} = number of variables).

Description	Fit no.	R_{factor}	$\chi^2{}_\nu$	χ^2	N_{var}	N_{idp}	ν	$1+2\sqrt{2/\nu}$
N_4	1	0.0602	138.881	575.461	3	7	4	2.4
N_5	2	0.0283	65.259	270.404	3	7	4	2.4
N_6	3	0.0192	44.259	183.391	3	7	4	2.4
N_7	4	0.0262	60.38	250.186	3	7	4	2.4
N_2N_2	5	0.0318	142.003	304.392	5	7	2	3.0
N_3N_1	6	0.0334	148.895	319.165	5	7	2	3.0
N_4N_1	7	0.017	75.827	162.539	5	7	2	3.0
N_3N_2	8	0.016	71.473	153.207	5	7	2	3.0
N_5N_1	9	0.0151	67.316	144.296	5	7	2	3.0
N_4N_2	10	0.0146	65.111	139.568	5	7	2	3.0
N_3N_3	11	0.0143	63.994	137.175	5	7	2	3.0
N_6S_1	12	0.0179	79.673	170.783	5	7	2	3.0
N_5S_1	13	0.0155	69.288	148.523	5	7	2	3.0
N_4S_1	14	0.0229	102	218.642	5	7	2	3.0
N_3S_1	15	0.0426	190.287	407.89	5	7	2	3.0

Table S4 Ni-*Hp*UreE H152A EXAFS fits using multiple-scattering imidazoles

Fits were carried out in r-space ($\Delta k = 2$–13.5 Å^{-1}; $\Delta r = 1$–4.0 Å) with a Kaiser–Bessel window (d$k = 2$), k-weight = 3 and $S_0 = 0.9$. All paths with an amplitude of 14% or higher and a R_{eff} within the fitting range were included for the imidazoles. Separate sets of Δr_{eff} and σ^2 for the histidine ligands (modelled as imidazoles 'H$^\alpha$', where α is the angle of rotation) and nitrogen atoms were used with initial values of 0.0 Å and 0.003 Å^2 respectively; with a universal E_0 initially set to 8340.0 eV and $\Delta E_0 = 0$ eV. Initial input metal–ligand distances were 2.0 Å for Ni – imidazole and 2.0 Å for Ni–N (where $\nu = N_{idp} - N_{var}$; N_{idp} = number of independent points, and N_{var} = number of variables).

Description	Fit no.	R_{factor}	$\chi^2{}_\nu$	χ^2	ΔE	N_{var}	N_{idp}	ν	$1+2\sqrt{2/\nu}$
$N_5H_1{}^5$	16	0.0631	39.547	664.307		3	19	16	1.7
$N_4H_2{}^5$	17	0.0597	37.394	628.132		3	19	16	1.7
$N_3H_3{}^5$	18	0.0741	46.45	780.254		3	19	16	1.7
$N_2H_4{}^5$	19	0.1044	65.385	1098.33		3	19	16	1.7
$N_4H_2{}^5$	20	0.0553	39.327	581.95		5	19	14	1.8
$N_4H_2{}^{10}$	21	0.0534	33.449	561.875		3	19	16	1.7
$N_4H_2{}^{10}$	22	0.0518	32.427	544.706		3	19	16	1.7
$N_1N_3H_2{}^{10}$	23	0.0497	35.344	523.02		5	19	14	1.8
$N_4H_2{}^5$	17	0.0597	37.394	628.132	2.56	3	19	16	1.7
N	4 N/O	2 N_{His}							
r (Å)	2.09(1)	2.09(1)							
σ^2 ($\times 10^3$)	3.3(1)	3.3(1)							
$N_4H_2{}^5$	20	0.0553	39.327	581.95	1.02	5	19	14	1.8
N	4 N/O	2 N_{His}							
r (Å)	2.10(1)	2.07(3)							
σ^2 ($\times$ 10^3)	3(1)	4(3)							
$N_4H_2{}^{10}$	22	0.0518	32.427	544.706	0.71	3	19	16	1.7
N	4 N/O	2 N_{His}							
r (Å)	2.09(1)	2.09(1)							
σ^2 ($\times 10^3$)	3.7(5)	3.7(5)							
$N_1N_3H_2{}^{10}$	23	0.0497	35.344	523.02	1.39	5	19	14	1.8
N	1 N/O	3 N/O	2 N_{His}						
r (Å)	2.13(3)	2.06(2)	2.13(3)						
σ^2 ($\times 10^3$)	2(2)	2(2)	4(3)						

Table S5 Zn-*Hp*UreE wild-type single-scattering EXAFS fits

Fits were carried out in r-space ($\Delta k = 2$–13.5 Å^{-1}; $\Delta r = 1$–2.5 Å) with a Kaiser–Bessel window (d$k = 2$), k-weight = 3 and $S_0 = 0.9$. Three separate sets of Δr_{eff} and σ^2 for the sulfur atoms, nitrogen ligands and bromide ions were used with initial values of 0.0 Å and 0.003 Å^2 respectively. A universal E_0 was initially set to 9670.0 eV and $\Delta E_0 = 0$ eV. Initial input metal–ligand distances were 2.0 Å for Zn–N, 2.3 Å for Zn–S and 2.4 Å for Zn–Br (where $\nu = N_{idp} - N_{var}$; N_{idp} = number of independent points, and N_{var} = number of variables).

Description	Fit no.	R_{factor}	$\chi^2{}_\nu$	χ^2	N_{var}	N_{idp}	ν	$1+2\sqrt{2/\upsilon}$
N_3	2	0.5058	439.11	3396.24	3	10	7	2.1
N_4	3	0.4769	414.062	3202.509	3	10	7	2.1
N_4	4	0.473	410.612	3175.829	3	10	7	2.1
N_6	5	0.4835	419.795	3246.848	3	10	7	2.1
N_7	6	0.502	435.813	3370.744	3	10	7	2.1
S_2	7	0.4153	360.52	2788.396	3	10	7	2.1
S_3	8	0.3886	337.374	2609.376	3	10	7	2.1
S_4	9	0.3883	337.067	2607.003	3	10	7	2.1
S_5	10	0.4017	348.758	2697.424	3	10	7	2.1
S_6	11	0.4214	365.819	2829.381	3	10	7	2.1
S_7	12	0.4431	384.708	2975.475	3	10	7	2.1
Br_1	13	0.4015	348.593	2696.149	3	10	7	2.1
Br_2	14	0.3535	306.871	2373.452	3	10	7	2.1
Br_3	15	0.3373	292.873	2265.191	3	10	7	2.1
Br_4	16	0.331	287.348	2222.459	3	10	7	2.1
Br_5	17	0.3268	283.73	2194.477	3	10	7	2.1
Br_6	18	0.3228	280.264	2167.669	3	10	7	2.1
Br_7	19	0.3199	277.733	2148.093	3	10	7	2.1
N_2N_1	20	0.2552	298.877	1713.871	5	10	5	2.3
N_2N_2	21	0.284	332.57	1907.081	5	10	5	2.3
N_3N_1	22	0.2572	301.131	1726.801	5	10	5	2.3
N_4N_1	23	0.4647	544.193	3120.609	5	10	5	2.3
N_3N_2	24	0.3161	370.193	2122.824	5	10	5	2.3
N_5N_1	25	0.4491	525.887	3015.63	5	10	5	2.3
N_3N_3	26	0.3878	454.139	2604.202	5	10	5	2.3
N_6N_1	27	0.4628	541.882	3107.356	5	10	5	2.3
N_5N_2	28	0.4607	539.42	3093.235	5	10	5	2.3
N_4N_3	29	0.4618	540.699	3100.573	5	10	5	2.3
S_2S_1	30	0.1625	190.23	1090.849	5	10	5	2.3
S_2S_2	31	0.0896	104.921	601.654	5	10	5	2.3
S_3S_1	32	0.2296	268.898	1541.96	5	10	5	2.3
S_4S_1	33	0.3815	446.761	2561.895	5	10	5	2.3
S_3S_2	34	0.2862	335.141	1921.825	5	10	5	2.3
S_5S_1	35	0.392	459.061	2632.429	5	10	5	2.3
S_4S_2	36	0.3789	443.639	2543.991	5	10	5	2.3
S_3S_3	37	0.3459	405.057	2322.751	5	10	5	2.3
S_6S_1	38	0.4214	493.407	2829.381	5	10	5	2.3
S_5S_2	39	0.3904	457.178	2621.631	5	10	5	2.3
S_4S_3	40	0.3765	440.875	2528.142	5	10	5	2.3
N_2S_1	41	0.1663	194.778	1116.932	5	10	5	2.3
N_1S_2	42	0.2281	267.059	1531.419	5	10	5	2.3
N_2S_2	43	0.2907	340.454	1952.29	5	10	5	2.3
N_3S_1	44	0.2148	251.528	1442.355	5	10	5	2.3
N_1S_3	45	0.3179	372.289	2134.844	5	10	5	2.3
N_1S_4	46	0.3878	454.1	2603.979	5	10	5	2.3
N_4S_1	47	0.2712	317.515	1820.749	5	10	5	2.3
N_2S_3	48	0.3736	437.44	2508.447	5	10	5	2.3
N_3S_2	49	0.3528	413.09	2368.816	5	10	5	2.3
N_5S_1	50	0.3224	377.464	2164.52	5	10	5	2.3
N_1S_5	51	0.398	466.076	2672.654	5	10	5	2.3
N_4S_2	52	0.3144	368.156	2111.147	5	10	5	2.3
N_2S_4	53	0.1486	174.017	997.879	5	10	5	2.3
N_3S_3	54	0.3678	430.728	2469.957	5	10	5	2.3
N_6S_1	55	0.3595	420.976	2414.033	5	10	5	2.3
N_1S_6	56	0.409	478.95	2746.478	5	10	5	2.3
N_3S_4	57	0.3749	439.032	2517.577	5	10	5	2.3
N_5S_2	58	0.2922	342.111	1961.793	5	10	5	2.3
N_2S_5	59	0.1511	176.945	1014.666	5	10	5	2.3
N_4S_3	60	0.3585	419.741	2406.953	5	10	5	2.3
S_2Br_1	61	0.0789	92.371	529.69	5	10	5	2.3
S_2Br_2	62	0.1334	156.249	895.988	5	10	5	2.3
S_3Br_1	63	0.1164	136.352	781.892	5	10	5	2.3
S_4Br_1	64	0.1538	180.095	1032.735	5	10	5	2.3
S_3Br_2	65	0.2087	244.409	1401.532	5	10	5	2.3
S_5Br_1	66	0.1839	215.368	1235.003	5	10	5	2.3
S_4Br_2	67	0.2005	234.814	1346.514	5	10	5	2.3

Table S5 Continued

Description	Fit no.	R_{factor}	χ^2_ν	χ^2	N_{var}	N_{idp}	ν	$1+2\sqrt{2/\nu}$
S_3Br_3	68	0.2001	234.256	1343.312	5	10	5	2.3
S_6Br_1	69	0.2052	240.255	1377.714	5	10	5	2.3
S_5Br_2	70	0.1956	229.086	1313.668	5	10	5	2.3
S_4Br_3	71	0.1882	220.41	1263.912	5	10	5	2.3
N_2Br_1	72	0.0328	38.434	220.393	5	10	5	2.3
N_1Br_2	73	0.0784	91.768	526.234	5	10	5	2.3
N_2Br_2	74	0.0607	71.128	407.877	5	10	5	2.3
N_3Br_1	75	0.025	29.293	167.979	5	10	5	2.3
N_1Br_3	76	0.103	120.615	691.653	5	10	5	2.3
N_1Br_4	77	0.1345	157.507	903.204	5	10	5	2.3
N_4Br_1	78	0.0357	41.845	239.956	5	10	5	2.3
N_2Br_3	79	0.1046	122.437	702.1	5	10	5	2.3
N_3Br_2	80	0.0703	82.291	471.886	5	10	5	2.3
N_5Br_1	81	0.0532	62.239	356.902	5	10	5	2.3
N_1Br_5	82	0.1662	194.665	1116.28	5	10	5	2.3
N_4Br_2	83	0.0832	97.403	558.545	5	10	5	2.3
N_2Br_4	84	0.1464	171.486	983.366	5	10	5	2.3
N_3Br_3	85	0.1178	137.972	791.182	5	10	5	2.3
N_6Br_1	86	0.0717	83.944	481.365	5	10	5	2.3
N_1Br_6	87	0.196	229.564	1316.404	5	10	5	2.3
N_5Br_2	88	0.0921	107.822	618.293	5	10	5	2.3
N_2Br_5	89	0.1831	214.432	1229.636	5	10	5	2.3
N_4Br_3	90	0.1189	139.268	798.614	5	10	5	2.3
N_3Br_4	91	0.1522	178.266	1022.242	5	10	5	2.3
$N_2S_1Br_1$	92	0.0197	35.445	132.363	7	10	3	2.6
$N_1S_2Br_1$	93	0.0339	60.972	227.691	7	10	3	2.6
$N_1S_1Br_2$	94	0.0264	47.479	177.303	7	10	3	2.6
$N_3S_1Br_1$	95	0.0182	32.642	121.896	7	10	3	2.6
$N_1S_3Br_1$	96	0.0315	56.567	211.242	7	10	3	2.6
$N_1S_1Br_3$	97	0.0212	38.168	142.532	7	10	3	2.6
$N_4S_1Br_1$	98	0.0266	47.858	178.72	7	10	3	2.6
$N_1S_4Br_1$	99	0.0297	53.432	199.535	7	10	3	2.6
$N_1S_1Br_4$	100	0.0197	35.353	132.023	7	10	3	2.6
$N_2S_2Br_1$	101	0.0172	30.859	115.241	7	10	3	2.6
$N_2S_1Br_2$	102	0.0162	29.068	108.549	7	10	3	2.6
$N_1S_2Br_2$	103	0.0197	35.481	132.498	7	10	3	2.6
$N_3S_2Br_1$	104	0.0171	30.765	114.889	7	10	3	2.6
$N_1S_3Br_2$	105	0.0161	29.015	108.352	7	10	3	2.6
$N_2S_1Br_3$	106	0.014	25.229	94.214	7	10	3	2.6
$N_3S_1Br_2$	107	0.0053	9.61	35.889	7	10	3	2.6
$N_1S_2Br_3$	108	0.0166	29.878	111.576	7	10	3	2.6
$N_2S_3Br_1$	109	0.0152	27.418	102.388	7	10	3	2.6
$N_2S_2Br_2$	110	0.0166	29.854	111.484	7	10	3	2.6
$N_2N_1Br_1$	111	0.0131	23.606	88.154	7	10	3	2.6
$N_2N_2Br_1$	112	0.0141	25.388	94.809	7	10	3	2.6
$N_3N_1Br_1$	113	0.0141	25.382	94.787	7	10	3	2.6
$N_4N_1Br_1$	114	0.0255	45.843	171.194	7	10	3	2.6
$N_3N_2Br_1$	115	0.0189	33.983	126.905	7	10	3	2.6
$N_3N_3Br_1$	116	0.3585	644.56	2407.03	7	10	3	2.6

Table S6 Zn-*Hp*UreF EXAFS fits using multiple-scattering imidazoles

Fits were carried out in r-space ($\Delta k = 2$–13.5 Å^{-1}; $\Delta r = 1$–4.1 Å) with a Kaiser–Bessel window (d$k = 2$), k-weight = 3 and $S_0 = 0.9$. All paths with an amplitude of 14% or higher and a r_{eff} within the fitting range were included for the imidazoles. Separate sets of Δr_{eff} and σ^2 for the sulfur atoms, nitrogen atoms, histidine ligands (modelled as imidazoles 'H$^{\alpha}$', where α is the angle of rotation) and bromide ions were used with initial values of 0.0 Å and 0.003 Å^2 respectively; with a universal E_0 initially set to 9670.0 eV and $\Delta E_0 = 0$ eV. Initial input metal–ligand distances were 2.0 Å for Zn–imidazole, 2.0 Å for Zn–N, 2.3 Å for Zn–S and 2.4 Å for Zn–Br (where $\nu = N_{idp} - N_{var}$; N_{idp} = number of independent points, and N_{var} = number of variables).

Description	Fit no.	R_{factor}	$\chi^2{}_\nu$	χ^2	ΔE	N_{var}	N_{idp}	ν	$1+2\sqrt{2/\nu}$
$N_2Br_1H_1{}^5$	117	0.0477	19.398	336.805		5	22	17	1.7
$N_1Br_1H_1{}^5$	118	0.0654	26.615	462.125		5	22	17	1.7
$N_3Br_1H_1{}^5$	119	0.0475	19.337	335.749		5	22	17	1.7
$N_5Br_1H_1{}^5$	120	0.0543	22.104	383.805		5	22	17	1.7
$N_0Br_1H_2{}^5$	121	0.0841	34.249	594.669		5	22	17	1.7
$N_1Br_1H_2{}^5$	122	0.0487	19.825	344.219		5	22	17	1.7
$N_2Br_1H_2{}^5$	123	0.0415	16.885	293.176		5	22	17	1.7
$N_3Br_1H_2{}^5$	124	0.0456	18.57	322.444		5	22	17	1.7
$N_0Br_1H_3{}^5$	126	0.0696	28.312	491.584		5	22	17	1.7
$N_1Br_1H_3{}^5$	127	0.0503	20.472	355.455		5	22	17	1.7
$N_2Br_1H_3{}^5$	128	0.0478	19.442	337.579		5	22	17	1.7
$N_3Br_1H_3{}^5$	129	0.0532	21.638	375.704		5	22	17	1.7
$N_0Br_1H_4{}^5$	130	0.0704	28.668	497.765		5	22	17	1.7
$N_2Br_1H_2{}^5$	131	0.0377	17.342	266.426		7	22	15	1.7
$N_2S_1H_2{}^5$	132	0.1708	78.557	1206.897		7	22	15	1.7
$N_1Br_1H_1{}^5H_2{}^5$	133	0.0337	15.523	238.484		7	22	15	1.7
$N_1Br_1H_2{}^5H_2{}^5$	134	0.0444	20.432	313.91		7	22	15	1.7
$N_0Br_1H_2{}^5H_2{}^5$	135	0.0451	20.753	318.842		7	22	15	1.7
$N_2Br_1H_1{}^5H_2{}^5$	136	0.0288	15.219	203.38		9	22	13	1.8
$N_1Br_1H_1{}^5H_2{}^5$	137	0.0244	12.91	172.514		9	22	13	1.8
$N_1Br_1H_2{}^5H_2{}^5$	138	0.0261	12.841	184.438		8	22	14	1.8
$N_2Br_1H_2{}^5$	131	0.0377	17.342	266.426	− 5.31	7	22	15	1.7
N	2 N/O	2 N_{His}	1 Br						
r (Å)	2.07(3)	1.99(2)	2.38(1)						
σ^2 ($\times 10^3$)	12(5)	5(1)	4.3(4)						
$N_1Br_1H_1{}^5H_2{}^5$	133	0.0337	15.523	238.484	− 1.85	7	22	15	1.7
N	1 N/O	1 Br	1 N_{His}	2 N_{His}					
r (Å)	1.98(1)	2.39(1)	1.98(1)	2.12(2)					
σ^2 ($\times 10^3$)	2(1)	4.7(4)	2(1)	5(2)					
$N_1Br_1H_1{}^5H_2{}^5$	137	0.0244	12.91	172.514	− 2.92	9	22	13	1.8
N	1 N/O	1 Br	1 N_{His}	2 N_{His}					
r (Å)	2.02(2)	2.39(1)	2.16(1)	1.99(2)					
σ^2 ($\times 10^3$)	3(2)	4.9(5)	1(1)	4.8(5)					
$N_1Br_1H_1{}^5H_2{}^5$	138	0.0261	12.841	184.438	− 2.65	8	22	14	1.8
N	1 N/O	1 Br	1 N_{His}	2 N_{His}					
r (Å)	2.00(1)	2.39(1)	2.16(1)	2.00(1)					
σ^2 ($\times 10^3$)	3(2)	4.8(5)	1(1)	4(1)					

Table S7 Zn-*Hp*UreE H152A single-scattering fits

Fits were carried out in r-space ($\Delta k = 2$–13.5 Å^{-1}; $\Delta r = 1$–2.5 Å) with a Kaiser–Bessel window (d$k = 2$), k-weight = 3 and $S_0 = 0.9$. Three separate sets of Δr_{eff} and σ^2 for the sulfur atoms, nitrogen ligands and bromide ions were used with initial values of 0.0 Å and 0.003 Å^2 respectively. A universal E_0 was initially set to 9670.0 eV and $\Delta E_0 = 0$ eV. Initial input metal–ligand distances were 2.0 Å for Zn–N, 2.3 Å for Zn–S and 2.4 Å for Zn–Br (where $\nu = N_{idp} - N_{var}$; N_{idp} = number of independent points, and N_{var} = number of variables).

Description	Fit no.	R_{factor}	$\chi^2{}_\nu$	χ^2	N_{var}	N_{idp}	ν	$1+2\sqrt{2/\nu}$
N_2	1	0.6239	286.971	2219.541	3	10	7	2.1
N_3	2	0.5593	257.247	1989.646	3	10	7	2.1
N_4	3	0.5323	244.825	1893.567	3	10	7	2.1
N_5	4	0.5286	243.151	1880.621	3	10	7	2.1
N_6	5	0.539	247.916	1917.478	3	10	7	2.1
N_7	6	0.5571	256.228	1981.763	3	10	7	2.1
S_2	7	0.429	197.307	1526.048	3	10	7	2.1
S_3	8	0.4125	189.729	1467.439	3	10	7	2.1
S_4	9	0.4136	190.22	1471.235	3	10	7	2.1
S_5	10	0.4277	196.729	1521.575	3	10	7	2.1
S_6	11	0.4483	206.186	1594.718	3	10	7	2.1
S_7	12	0.4712	216.728	1676.254	3	10	7	2.1
Br_1	13	0.3725	171.356	1325.331	3	10	7	2.1
Br_2	14	0.3205	147.439	1140.348	3	10	7	2.1
Br_3	15	0.304	139.839	1081.569	3	10	7	2.1
Br_4	16	0.2996	137.818	1065.935	3	10	7	2.1
Br_5	17	0.3008	138.348	1070.034	3	10	7	2.1
Br_6	18	0.3045	140.07	1083.353	3	10	7	2.1
N_2N_1	19	0.3091	191.758	1099.61	5	10	5	2.3
N_2N_2	20	0.3435	213.104	1222.019	5	10	5	2.3
N_3N_1	21	0.3136	194.555	1115.651	5	10	5	2.3
N_4N_1	22	0.4346	269.621	1546.108	5	10	5	2.3
N_3N_2	23	0.3754	232.911	1335.596	5	10	5	2.3
N_5N_1	24	0.0821	50.942	292.12	5	10	5	2.3
N_4N_2	25	0.4223	261.978	1502.28	5	10	5	2.3
N_3N_3	26	0.4482	278.051	1594.45	5	10	5	2.3
N_6N_1	27	0.0894	55.48	318.145	5	10	5	2.3
N_5N_2	28	0.5112	317.168	1818.759	5	10	5	2.3
N_4N_3	29	0.5447	337.929	1937.812	5	10	5	2.3
S_2S_1	30	0.1704	105.723	606.258	5	10	5	2.3
S_2S_2	31	0.2103	130.458	748.095	5	10	5	2.3
S_3S_1	32	0.2367	146.845	842.062	5	10	5	2.3
S_4S_1	33	0.3979	246.867	1415.631	5	10	5	2.3
S_3S_2	34	0.2907	180.37	1034.312	5	10	5	2.3
S_5S_1	35	0.4018	249.256	1429.325	5	10	5	2.3
S_4S_2	36	0.3892	241.463	1384.64	5	10	5	2.3
S_3S_3	37	0.3511	217.823	1249.077	5	10	5	2.3
S_6S_1	38	0.4224	262.024	1502.546	5	10	5	2.3
S_5S_2	39	0.1704	105.723	606.258	5	10	5	2.3
S_4S_3	40	0.2526	156.713	898.653	5	10	5	2.3
N_2S_1	41	0.175	108.59	622.696	5	10	5	2.3
N_1S_2	42	0.2356	146.154	838.1	5	10	5	2.3
N_2S_2	43	0.2959	183.558	1052.592	5	10	5	2.3
N_3S_1	44	0.2228	138.229	792.657	5	10	5	2.3
N_1S_3	45	0.3303	204.895	1174.942	5	10	5	2.3
N_1S_4	46	0.4056	251.645	1443.029	5	10	5	2.3
N_4S_1	47	0.4056	251.645	1443.029	5	10	5	2.3
N_2S_3	48	0.3978	246.799	1415.239	5	10	5	2.3
N_3S_2	49	0.3978	246.799	1415.239	5	10	5	2.3
N_5S_1	50	0.3364	208.726	1196.915	5	10	5	2.3
N_1S_5	51	0.1283	79.593	456.417	5	10	5	2.3
N_4S_2	52	0.306	189.828	1088.543	5	10	5	2.3
N_2S_4	53	0.4006	248.557	1425.321	5	10	5	2.3
N_3S_3	54	0.1254	77.798	446.123	5	10	5	2.3
N_6S_1	55	0.3828	237.508	1361.958	5	10	5	2.3
N_1S_6	56	0.4392	272.475	1562.474	5	10	5	2.3
N_5S_2	57	0.2918	181.051	1038.216	5	10	5	2.3
N_2S_5	58	0.141	87.494	501.721	5	10	5	2.3
N_4S_3	59	0.1053	65.339	374.676	5	10	5	2.3
N_3S_4	60	0.1316	81.67	468.327	5	10	5	2.3
S_2Br_1	61	0.0558	34.602	198.42	5	10	5	2.3
S_2Br_2	62	0.1053	65.329	374.623	5	10	5	2.3
S_3Br_1	63	0.0879	54.559	312.862	5	10	5	2.3
S_4Br_1	64	0.1243	77.139	442.343	5	10	5	2.3
S_3Br_2	65	0.1519	94.233	540.369	5	10	5	2.3
S_4Br_2	66	0.1828	113.418	650.379	5	10	5	2.3

Table S7 Continued

Description	Fit no.	R_{factor}	χ^2_ν	χ^2	N_{var}	N_{idp}	ν	$1+2\sqrt{2/\nu}$
S_3Br_3	67	0.185	114.767	658.115	5	10	5	2.3
S_5Br_1	68	0.1565	97.07	556.637	5	10	5	2.3
S_6Br_1	69	0.1818	112.804	646.862	5	10	5	2.3
S_5Br_2	70	0.1822	113.005	648.015	5	10	5	2.3
S_4Br_3	71	0.1765	109.483	627.818	5	10	5	2.3
N_2Br_1	72	0.0219	13.566	77.791	5	10	5	2.3
N_1Br_2	73	0.0596	36.954	211.909	5	10	5	2.3
N_2Br_2	74	0.0332	20.58	118.014	5	10	5	2.3
N_3Br_1	75	0.0094	5.818	33.363	5	10	5	2.3
N_1Br_3	76	0.0774	48.033	275.441	5	10	5	2.3
N_1Br_4	77	0.1055	65.435	375.227	5	10	5	2.3
N_4Br_1	78	0.0183	11.332	64.983	5	10	5	2.3
N_2Br_3	79	0.0696	43.161	247.499	5	10	5	2.3
N_3Br_2	80	0.0382	23.689	135.839	5	10	5	2.3
N_5Br_1	81	0.0367	22.797	130.728	5	10	5	2.3
N_1Br_5	82	0.1357	84.2	482.834	5	10	5	2.3
N_4Br_2	83	0.0533	33.058	189.565	5	10	5	2.3
N_2Br_4	84	0.1085	67.328	386.084	5	10	5	2.3
N_3Br_3	85	0.0813	50.45	289.3	5	10	5	2.3
N_6Br_1	86	0.0584	36.242	207.824	5	10	5	2.3
N_1Br_6	87	0.1654	102.585	588.261	5	10	5	2.3
N_5Br_2	88	0.0695	43.125	247.295	5	10	5	2.3
N_2Br_5	89	0.1448	89.834	515.144	5	10	5	2.3
N_4Br_3	90	0.0939	58.239	333.966	5	10	5	2.3
N_4Br_3	91	0.1207	74.887	429.428	5	10	5	2.3
$N_2S_1Br_1$	92	0.0136	12.954	48.375	7	10	3	2.6
$N_1S_2Br_1$	93	0.0296	28.155	105.141	7	10	3	2.6
$N_1S_1Br_2$	94	0.0236	22.497	84.011	7	10	3	2.6
$N_3S_1Br_1$	95	0.0083	7.888	29.457	7	10	3	2.6
$N_1S_3Br_1$	96	0.0308	29.303	109.429	7	10	3	2.6
$N_1S_1Br_3$	97	0.0308	29.303	109.429	7	10	3	2.6
$N_4S_1Br_1$	98	0.011	10.52	39.285	7	10	3	2.6
$N_1S_4Br_1$	99	0.0323	30.745	114.815	7	10	3	2.6
$N_1S_1Br_4$	100	0.0136	12.91	48.212	7	10	3	2.6
$N_2S_2Br_1$	101	0.0137	13.041	48.701	7	10	3	2.6
$N_2S_1Br_2$	102	0.0119	11.31	42.234	7	10	3	2.6
$N_1S_2Br_2$	103	0.0186	17.755	66.303	7	10	3	2.6
$N_3S_2Br_1$	104	0.0081	7.708	28.785	7	10	3	2.6
$N_1S_3Br_2$	105	0.016	15.263	57	7	10	3	2.6
$N_2S_1Br_3$	106	0.0084	8.04	30.026	7	10	3	2.6
$N_3S_1Br_2$	107	0.0183	17.435	65.11	7	10	3	2.6
$N_1S_2Br_3$	108	0.0201	19.154	71.529	7	10	3	2.6
$N_2S_3Br_1$	109	0.0135	12.819	47.87	7	10	3	2.6
$N_2S_2Br_2$	110	0.0141	13.427	50.142	7	10	3	2.6

Table S8 Zn-*Hp*UreE H152A EXAFS fits using multiple-scattering imidazoles

Fits were carried out in r-space ($\Delta k = 2$–13.5 Å^{-1}; $\Delta r = 1$–4.1 Å) with a Kaiser–Bessel window (d$k = 2$), k-weight = 3 and $S_0 = 0.9$. All paths with an amplitude of 14% or higher and a r_{eff} within the fitting range were included for the imidazoles. Separate sets of Δr_{eff} and σ^2 for the sulfur atoms, nitrogen atoms, histidine ligands (modelled as imidazoles 'H$^{\alpha}$', where α is the angle of rotation) and bromide ions were used with initial values of 0.0 Å and 0.003 Å^2 respectively; with a universal E_0 initially set to 9670.0 eV and $\Delta E_0 = 0$ eV. Initial input metal–ligand distances were 2.0 Å for Zn–imidazole, 2.0 Å for Zn–N, 2.3 Å for Zn–S and 2.4 Å for Zn–Br (where $\nu = N_{idp} - N_{var}$; N_{idp} = number of independent points, and N_{var} = number of variables).

Description	Fit no.	R_{factor}	$\chi^2{}_\nu$	χ^2	ΔE	N_{var}	N_{idp}	ν	$1+2\sqrt{2/\nu}$
$N_1Br_1H_1{}^5$	111	0.0481	10.316	179.111		5	22	17	1.7
$N_2Br_1H_1{}^5$	112	0.0261	5.591	97.07		5	22	17	1.7
$N_3Br_1H_1{}^5$	113	0.0242	5.192	90.15		5	22	17	1.7
$N_4Br_1H_1{}^5$	114	0.0313	6.711	116.529		5	22	17	1.7
$N_3Br_1H_2{}^5$	115	0.0226	4.852	84.246		5	22	17	1.7
$N_2Br_1H_2{}^5$	116	0.0185	3.961	68.775		5	22	17	1.7
$N_1Br_1H_2{}^5$	117	0.0275	5.908	102.574		5	22	17	1.7
$N_0Br_1H_2{}^5$	118	0.0666	14.292	248.16		5	22	17	1.7
$N_0Br_1H_3{}^5$	119	0.0483	10.365	179.978		5	22	17	1.7
$N_1Br_1H_3{}^5$	120	0.0276	5.93	102.965		5	22	17	1.7
$N_2Br_1H_3{}^5$	121	0.0251	5.377	93.363		5	22	17	1.7
$N_3Br_1H_3{}^5$	122	0.0315	6.752	117.235		5	22	17	1.7
$N_2Br_1H_2{}^5$	116	0.0185	3.961	68.775	−3.9	5	22	17	1.7
N	2 N/O	2 N_{His}	1 Br						
r (Å)	2.01(1)	2.01(1)	2.391(4)						
σ^2 ($\times 10^3$)	6.7(5)	6.7(5)	3.4(2)						
$N_3Br_1H_2{}^5$	115	0.0226	4.852	84.246	−3.95	5	22	17	1.7
N	3 N/O	2 N_{His}	1 Br						
r (Å)	2.01(1)	2.01(1)	2.391(4)						
σ^2 ($\times 10^3$)	8.5(6)	8.5(6)	3.5(2)						

Received 13 September 2011/20 October 2011; accepted 20 October 2011
Published as BJ Immediate Publication 20 October 2011, doi:10.1042/BJ20111659